The Role of Ice Microphysics Parametrizations in Determining the Prevalence of Supercooled Liquid Water in High-Resolution Simulations of a Southern Ocean Midlatitude Cyclone

KALLI FURTADO AND PAUL FIELD

Met Office, Exeter, United Kingdom

(Manuscript received 31 May 2016, in final form 29 March 2017)

ABSTRACT

High-resolution simulations of a Southern Ocean cyclone are compared to satellite-derived observations of liquid water path, cloud-top properties, and top-of-atmosphere radiative fluxes. The focus is on the cold-air-outflow region, where there are contributions to the hydrological budget from the microphysical growth of ice particles by riming and vapor deposition and transport by turbulent mixing. The sensitivity of the simulation to the parameterization of these processes is tested and the relative importance of ice-nucleation temperature is identified. It is shown that ice-phase microphysics is a key factor determining the phase composition of Southern Ocean clouds and physically reasonable parameterization changes are identified that affect the liquid water content of these clouds. The information gained from the sensitivity tests is applied to global model development, where it is shown that a modification to the riming parameterization improves climate mean-state biases in the Southern Ocean region.

1. Introduction

The poor representation of mixed-phase clouds in models is a possible cause of the severe Southern Ocean radiation biases seen in many climate models (Bodas-Salcedo et al. 2012; Williams et al. 2013; Bodas-Salcedo et al. 2014) and is also key to understanding the predicted climate sensitivity of the planet (Ceppi et al. 2016; McCoy et al. 2015). Many general circulation models show large deficits (of up to $-40\,\mathrm{W\,m^{-2}}$ during the Southern Hemisphere summer) in the solar radiation reflected back to space over the Southern Ocean, compared to satellite measurements (Bodas-Salcedo et al. 2014). This top-of-atmosphere bias is accompanied by excessive transmission of solar radiation to the sea surface (Trenberth and Fasullo 2010; Bodas-Salcedo et al. 2012), which is related to the development of large sea surface temperature biases that are seen in many coupled atmosphere–ocean models (Sallée et al. 2013; Jones et al. 2016). Among other consequences, this leads to biases in the prediction of the high-latitude cryosphere (Turner et al. 2013) and may increase uncertainties in climate projections (He and Soden 2016).

By compositing midlatitude storms, in models and remotely sensed observations, Bodas-Salcedo et al. (2014) showed that these radiation biases occur mainly in cold-air-outbreak conditions and are correlated with the occurrence of low- and midlevel clouds. Moreover, remotely sensed estimates of cloud phase suggest that a significant fraction of the bias is due to underprediction of the liquid water contents of clouds that have supercooled liquid or mixed-phase tops (Williams et al. 2013; Bodas-Salcedo et al. 2016). This strongly implicates a role for subgrid-scale processes, particularly cold-cloud microphysics, in determining these biases. At the same time, the accurate simulation of mixed-phase clouds by models is a challenging problem (Klein et al. 2009) because of the physical complexity of mixed-phase clouds (Morrison et al. 2012). In part, this complexity arises from the web of microphysical processes that need to be parameterized to simulate mixed-phase environments. In this paper we will use high-resolution (convection permitting) simulations of a Southern Ocean cyclone to study the sensitivity of cold-sector clouds to the parameterization of the processes in the mixed-phase "web." The information gained by doing so will then be used to reduce the Southern Ocean shortwave flux bias in a climate model.

The role of microphysical processes in influencing the liquid water contents of mixed-phase clouds has been

Corresponding author: Kalli Furtado, kalli.furtado@metoffice.gov.uk

DOI: 10.1175/JAS-D-16-0165.1

studied from a number of standpoints. One aspect of the problem lies in the formulation of the source of liquid water in the presence of ice. For example, using theoretical models of mixed-phase environments, Korolev and Field (2008) and Field et al. (2014b) studied how turbulence competes with ice growth to determine the liquid cloud properties. The model of Field et al. (2014b) is analytically solvable and simple enough to be implemented in a general circulation model (Furtado et al. 2016), where it plays the role of a subgrid-scale, statistical cloud scheme for diagnosing liquid cloud fractions and water contents.

Another aspect of the maintenance of mixed-phase clouds in numerical models is the role played by cloud-microphysical processes in removing the liquid water diagnosed by the subgrid cloud scheme. For example, Huang et al. (2015a) investigated the phase and liquid water contents of Southern Ocean clouds in limited-area simulations performed with the Australian Community Climate and Earth-System Simulator (ACCESS). They found that combining changes to the diagnosis of boundary layer type and cloud-to-rain conversion improved the frequency of occurrence of liquid water, compared to in situ aircraft observations, although large discrepancies remained for the cases studied. In an earlier study, Huang et al. (2014) considered the impact of changing the entire cloud microphysics in Weather Research and Forecasting (WRF) Model simulations of Southern Ocean clouds, thereby obtaining the impact of convolving a large number of model differences, and evaluated these against observations. The models showed a lack of boundary layer cloud, which was linked to biases in surface fluxes. All the model configurations underestimated the liquid water contents and cloud cover associated with marine low clouds and compensated by overproduction of midlevel cloud tops.

The main sinks of liquid water in mixed-phase clouds are due to microphysical interactions with ice. For example, in an extensive study of the sensitivity of cloud phase to the microphysical parameters in the Community Atmosphere Model, version 5.0 (CAM5), Tan and Storelvmo (2016) found that the variability in supercooled liquid was dominated by the parameterization of the Bergeron–Findeisen process, whereby ice grows at the expense of liquid droplets. In this paper we will investigate how ice microphysics affects the phase properties and radiative impact of boundary layer clouds, using kilometer-scale simulations of a Southern Ocean cyclone performed with the Met Office Unified Model. The results are evaluated against satellite observations.

In mixed-phase environments, ice depletes water vapor by depositional growth and depletes liquid water by the accretion of droplets (riming). These processes either directly use up liquid water or modify the water vapor and temperature within cloud so that sustained condensation of liquid water becomes difficult and the cloud glaciates. Ice is also created in small quantities by nucleation. Once nucleated, these initially small quantities of ice may grow rapidly by vapor deposition and riming, leading to significant changes in the phase of the condensate. Simultaneous to these processes, ice is being removed by sedimentation and mixed by fluid turbulence.

Whether ice remains in a mixed-phase layer for a lengthy period of time, or rapidly sediments out, is determined by the balance between the ice-supplying processes (deposition, riming, nucleation, and turbulent mixing) and the ice-removing processes (sublimation, sedimentation, and turbulent mixing).

The aim of this paper is to study how the parameterizations of these processes influence the amounts of ice and liquid in boundary layer clouds in convection-permitting simulations of a Southern Ocean cyclone. Although the analysis is based on a single case, it can be used to understand how the model responds to parameterization changes and identify candidate changes that may alleviate climate model biases. We will assess the effects of the changes against measured top-of-atmosphere radiative fluxes and remotely sensed estimates of cloud-top properties (height, temperature, and phase) and cloud liquid water path. In this respect, the existence of large discrepancies between different satellite products for the Southern Ocean region (Huang et al. 2012, 2015a,b), for example, of up to 30% in cloud-top phase (Bodas-Salcedo et al. 2016), means that we can make few definitive statements about which physics configurations give the best performance. However, the data used at least provides a set of ''best estimates'' and a context within which to consider the model sensitivity experiments and may be used to make some tentative, qualitative statements about model performance. The understanding gained from assessment of the parameterization changes in high-resolution simulations can then be used to select candidate changes for implementation in coarser-resolution climate models. The advantage of developing microphysics parameterization changes at high resolution is that their effects can be isolated, without having to consider interactions with convection parameterizations or prognostic cloud-fraction schemes. The disadvantage is that convection-permitting models can show biases that are different from those found in climate models.

As a set of ''first guesses'' we have the following hypotheses as to how the system should respond to changes in the parameterization of riming, deposition, and ice nucleation. First, decreasing the efficiency of riming—that is, changing the parameterization so that for a given

mass of liquid and ice the riming rate is reduced—is expected to lead to higher liquid water contents because the accretion of liquid by ice proceeds more slowly. To a lesser extent, depositional growth and riming may also affect the thermal budget via latent heating.

Changes in deposition rate affect liquid water via their influence on the amount of "total water" (liquid plus vapor) in the system. As an example, consider modifying the deposition rates such that ice grows less rapidly by deposition: a change of this kind should increase the liquid water content because the net sink of water vapor is weaker, making it easier for the cloud scheme to diagnose condensation.

Finally, changing ice-nucleation temperature is expected to affect how much mixed-phase cloud exists in the system. Given that the amount of ice "seeded" by an initial nucleation event is very small, ice nucleation can only affect liquid water content via the subsequent depositional growth of the seeded ice particles. In the real world, this is likely to be very rapid for ice embedded in liquid water cloud. For the simulations considered here, however, we will see that initial ice growth is very sensitive to the details of how the deposition-rate and ice-nucleation parameterizations interact.

An outline of the paper is as follows. After introducing the atmospheric model and case study in sections 2 and 3, the parameterization changes to be investigated are described in section 4 and compared to remotely sensed measurements in section 5. In section 6 we consider the relevance of the high-resolution modeling results for global model development by assessing the effect of the riming-parameterization change on a local-area simulation, performed with a global model configuration, and on a 20-yr-long simulation using the methodology of the Atmospheric Model Intercomparison Project (AMIP). Section 7 discusses the findings in the context of existing ideas about the role of ice in hydrology of mixed-phase boundary layers. Section 8 offers some conclusions and prospects for future work.

2. Model description

The model used for the simulations is a nested, high-resolution model based on a previously operational version of the Met Office high-resolution forecasting model.

The high-resolution domain has an angular grid spacing of 0.02°, in a rotated latitude–longitude grid, giving a horizontal resolution of approximately 2.2 km over most of the domain. At this resolution convection is predominantly resolved by the model's nonhydrostatic dynamical core and no convection parameterization is used. The model has 80 nonuniformly spaced vertical levels, the highest of which is 38.5 km above the surface.

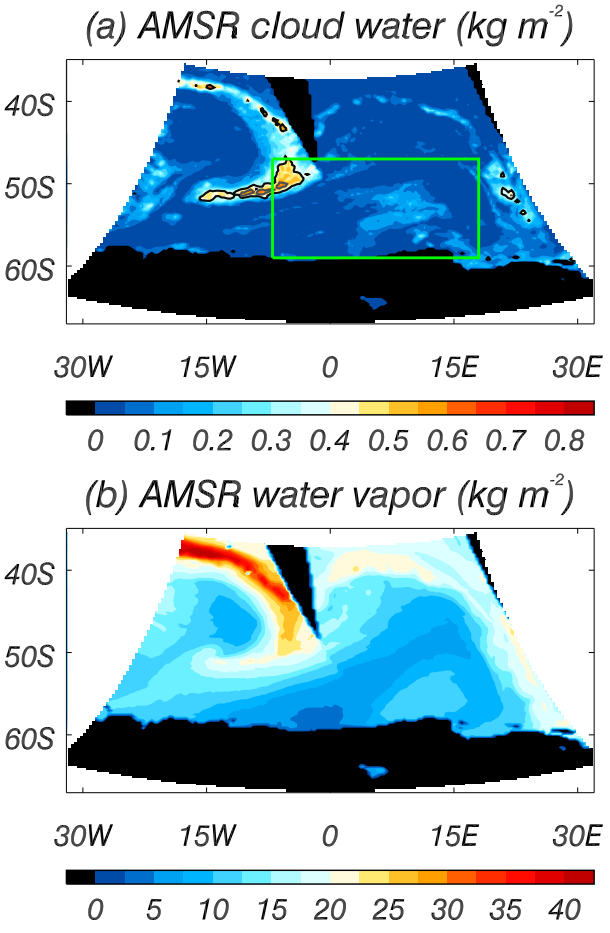

FIG. 1. (a) AMSR2 liquid cloud water path and (b) water vapor path, within the domain of the high-resolution model. The solid contours in (a) show AMSR2 surface rain rates of 1.5 (black) and 5 mm h^{-1} (gray). The blacked-out regions indicate missing data. The green box outlines the region, around the cold-air outflow, that will be analyzed.

The vertical resolution in the boundary layer is relatively high, with 16 model levels between the surface and 1.25 km and a grid spacing that varies from 5 m at the surface to around 150 m at 1.25 km. The boundary layer parameterization is the nonlocal scheme described by Lock et al. (2000) and operates throughout the depth of the model. To make use of the results of previous work on cold-air outbreaks, we include a change to the diagnosis of shear-dominated boundary layers described in Field et al. (2014a). The effect of this change is to increase the amount of stratiform cloud within the domain. Ice cloud fractions and subgrid moisture variability are diagnosed using the cloud scheme documented by Wilson et al. (2008).

The domain is centered on 52°S, 0°, and has 1500 × 1500 grid points in the azimuthal and polar directions. Figure 1a shows the lateral extent of the high-resolution

domain. The model time step is 50 s. The lateral boundary conditions for the domain are updated hourly from an N512 global model simulation performed with a model based on the Met Office Global Atmosphere 6.1 (GA6.1) configuration. The microphysics scheme (Wilson and Ballard 1999) uses mass mixing ratios as the prognostic moment for representing cloud droplets, rain, graupel, and snow. Where a process rate depends on other moments of a hydrometeor size distribution, these moments are diagnosed using an assumed distribution function. For snow, the size distribution is the moment-estimation parameterization of Field et al. (2007). The snow field includes all frozen hydrometeor mass, apart from graupel. The microphysical properties of the ice phase are described in Furtado et al. (2015, their "Model W") and in the papers referenced therein. Ice can sediment and grows by riming and deposition. Ice nucleation occurs heterogeneously below a threshold temperature (the default value of which is −10°C) and by homogeneous freezing for temperatures colder than −40°C. The heterogeneous nucleation parameterization is based on Fletcher (1962) and produces a seed mass of ice according to an exponential function of temperature. The mass of ice created is necessarily very small. For example, at a temperature of −10°C a mass of approximately 10^{-11} kg kg^{-1} is produced. However, in a water-saturated environment this small mass of ice should grow rapidly. To make the ice microphysics the same in the global model and the high-resolution model, we also use the microphysical properties from Furtado et al. (2015) in the global model simulations.

To investigate how the biases in the high-resolution simulations relate to those in climate models, we also ran simulations with a low-resolution, local-area model (LAM). The low-resolution model has a horizontal grid spacing of 0.2° (approximately 22 km) and uses the same model configuration as the global driving model. It is therefore configured to be typical of global numerical weather prediction (NWP) and climate models. The configuration has many differences from the high-resolution setup, including the use of a convection parameterization and a prognostic cloud-fraction scheme. We will use the low-resolution LAM to assess the effect of model configuration on the Southern Ocean cloud biases and to compare the effects of one of the parameterization changes across resolutions.

3. Case study description

To test the effects of the parameterization changes a midlatitude storm over the Southern Ocean on 9 December 2014 was chosen. For each model configuration, a simulation was initialized at 0000 UTC 9 December 2014 from an operational Met Office global model analysis. The same case was also examined in Bodas-Salcedo et al. (2016). The cyclone had an extensive stratiform cloud deck in the cold-air outflow behind of the cold front. Figure 1a shows the Advanced Microwave Scanning Radiometer 2 (AMSR2) cloud liquid water path (Wentz et al. 2014) at 1300 UTC, within the high-resolution model domain. The stratiform cloud is present in the area 50°–60°S, 0°–15°E, within the region shown by the green box. Figure 1b shows the AMSR2 water vapor path. The stratiform cloud lies within the relatively dry air behind a cold front that is advancing toward the northeast. The liquid water and water vapor in the front can be seen extending in a narrow arc across the top-left quadrants of Figs. 1a and 1b. In the northwest of the domain, a second frontal system is also present. The black regions show where no AMSR2 data are available owing to either a lack of satellite coverage or the presence of sea ice (on the southern extremity of the domain).

4. Descriptions of the sensitivity tests

The amounts of ice and liquid present may be influenced by turbulent mixing, depositional growth, riming, and ice nucleation. We investigate a set of changes that are expected to have a significant impact on each of these processes. The formulation of the model's "dynamical core" (e.g., the numerical method used to advect cloud species) will not be considered here but may be another factor.

In section 4a we examine the effects of changing the turbulent mixing, depositional growth, and riming rates of ice. In section 4b we examine the effects of changing ice-nucleation temperature.

A nomenclature for referring to the experiments and a summary of the configurations tested are given in Table 1. Throughout, the expression "+expt" is used to refer to a model configuration built from the control model by adding the configuration changes named "expt."

a. *Turbulent mixing of ice*

As an example of an extreme sensitivity, we investigate the effect of shutting off turbulent transport of ice entirely. This implies that ice is advected by the resolved-scale velocity field but is not mixed by the boundary layer scheme.

The physical motivation for considering this limiting case is that, because of the broad spectrum of ice crystal sizes, diffusive mixing by turbulence of the whole population of ice particles may not be appropriate. In reality, the motion of particles becomes increasingly influenced by inertia as particle size

TABLE 1. Summary of model configurations.

Configuration name	Resolution (km)	Description
Control	2.2 (0.02°)	High-resolution control
+mix	2.2	No boundary layer mixing of ice
+rime	2.2	Area-dependent riming with threshold LWC
+dep	2.2	Simplified subgrid vapor partitioning
+combined	2.2	Combination of all changes
+Tn = 0	2.2	Ice-nucleation temperature $T_n = 0$°C
+Tn = 0 (mod)	2.2	$T_n = 0$°C and modified process order
+Tn = 0 (mod) +combined	2.2	+combined with $T_n = 0$°C and modified process order
GLM	22 (0.2°)	Low-resolution control (based on GA6.1)
GLM+rime	22	GLM plus riming change

increases. For example, the rain species is not mixed by the boundary scheme because it is assumed that falling rain drops are not strongly influenced by subgrid-scale turbulence.

b. *Depositional growth of ice*

The microphysics scheme partitions each grid box into clear-sky, liquid-only, mixed-phase, and ice-only subgrid regions, based on an assumption of minimum overlap between liquid and ice cloud. To calculate the depositional growth rates of ice, the default microphysics uses a parameterization for the relative humidity (RH) in the ice-only cloud part of each grid box.

The parameterization assumes there is more water vapor in the ice-only cloud than in the clear sky. This contains an implicit assumption about the subgrid-scale correlations between ice water content (IWC) and RH. We investigate the effect of assuming that the RH is the same in the ice-only cloud and in the clear sky—that is, that the location of the ice within each grid box is uncorrelated with the subgrid RH fluctuations.

In more detail, the diagnosis of in–ice cloud RH is done as follows. Because any water cloud is assumed to be water saturated, the in–ice cloud specific humidity $q_{v,i}$ is given by

$$q_{v,i} = \frac{q_v - \phi_l q_{s,w} - \phi_c q_c}{\phi_i}, \tag{1}$$

where q_v is the gridbox mean specific humidity, $q_{s,w}$ is the saturated specific humidity with respect to water, q_c is the clear-sky specific humidity, and ϕ_c, ϕ_l, and ϕ_i are the clear-sky, liquid, and ice-only cloud fractions, respectively. The liquid cloud fraction ϕ_l includes any mixed-phase cloud, which is therefore assumed to be at water saturation. The clear-sky specific humidity is parameterized as

$$q_c = \frac{(q_v - \phi_l q_{s,w})}{1 - \phi_l} - w\phi_i, \tag{2}$$

where w is a decreasing function of the ice mass mixing ratio, q, and the critical relative humidity (RH_c) from the model's cloud scheme:

$$w = (1 - \mathrm{RH}_c) q_{s,w} \left(1 - A \frac{q}{q_{s,w}}\right), \tag{3}$$

for a given value of the constant A. Because of the complexity of the above parameterization, in particular, the ad hoc nature of the function w, a simple alternative is to choose w to be zero, which is equivalent to assuming that the in–ice cloud and clear-sky specific humidities are equal and given by Eq. (2) with $w = 0$. From Eq. (2) it can be seen that this choice of w maximizes the clear-sky relative humidity, for a given ice cloud fraction, and therefore minimizes the in–ice cloud RH.

Because the parameterization change decreases the RH diagnosed in the ice-only cloud, the expected effect of the changes is to reduce the deposition rates and thereby increase the amount of liquid water cloud. Note that only the diagnosed subgrid-scale partitioning of RH is altered by this change; the actual gridbox mean humidity is unaffected.

In addition, the microphysics scheme subdivides the ice-only cloud into sublimating and depositing parts, in which the depositional capacitance for ice growth is slightly different (10% lower for growing ice crystals, compared to sublimating ones). The rationale behind this is to account for the more rounded shapes of sublimating ice crystals. To further simplify the subgrid assumptions for ice growth, we will also remove this splitting. This further partitioning is also rather artificial; for example, the fractional subvolumes of the ice cloud are diagnosed by increasing or decreasing $\phi_i/2$ by an amount that depends linearly on the departure of $q_{v,i}$ from ice saturation. Separate tests, not shown here, demonstrate that removing this further subdivison is much less important than using the same average RH in the ice-only and clear-sky parts of the grid boxes.

c. Riming of ice crystals

The default riming parameterization assumes spherical ice particles. We test a parameterization that accounts for ice crystal shape. This is done by parameterizing ice crystal cross-sectional area in terms of diameter and using this area in the riming rates. As an example, we will use the area ratio–to–crystal diameter relationship from Heymsfield and Miloshevich [2003, their Eq. (2)]:

$$A_r = 0.051 D^{-0.2707}, \tag{4}$$

where A_r is the ratio of the ice crystal projected area to that of a spherical particle of the same diameter D. In each model grid box, the IWC is distributed over the values of the particle diameter D using the size-distribution parameterization of Field et al. (2007). The riming rate is therefore obtained by integrating the particle projected areas over this distribution.

In the default riming parameterization, all the in-cloud liquid water content (LWC) is available for accretion by ice. In reality, small water droplets may have very low collection efficiency (e.g., Harimaya 1975). To mimic this dependency, we "protect" some of the liquid from accretion by only using the excess, in-cloud LWC over a threshold of $10^{-4}\,\mathrm{kg\,kg^{-1}}$ to calculate riming. This value is based on the observation by Harimaya (1975) that droplets with diameters less than $10\,\mu$m are too small to be collected onto ice crystals, along with typical number concentrations for mixed-phase clouds from the in situ measurements of Korolev et al. (2003). The expected effect of this combination of changes is to reduce the efficiency of the riming process and thereby enhance liquid water content.

d. Heterogeneous ice nucleation

In section 4b we investigate the effects of ice-nucleation parameterization on liquid and ice water contents. It will be shown that the impact of ice nucleation on the model clouds is strongly dependent on assumptions in the parameterizations about the subgrid-scale spatial distribution of ice water content. In this section, it is argued that, for the Unified Model microphysics, these assumptions are implicit in the ordering of processes within each time step. Ice is nucleated by freezing small amounts of liquid water when the temperature is below a threshold. The default threshold is $T_n = -10$°C. A comparison to the MODIS cloud-top temperature, discussed in section 5a(1), shows that for this case this temperature is attained in pockets near to the stratiform cloud top. We will examine the effects of setting $T_n = 0$°C, which is warm enough for ice nucleation throughout the cloud layer.

For calculating deposition rates of ice, the air in any mixed-phase cloud is assumed to be saturated with respect to liquid water. Because ice nucleation increases the mixed-phase cloud fraction, the importance of ice nucleation may depend on the order in which nucleation and deposition occur, within a time step.

In the default microphysics, the subgrid-scale partitioning of relative humidity between cloudy regions (as described in section 4b) is calculated before ice nucleation. Therefore, any increase in mixed-phase cloud fraction due to ice nucleation will not affect the deposition rates until the next time step.

We will test the effect of calculating the subgrid humidity partition after ice nucleation has occurred. With this ordering of processes, any mixed-phase cloud created by ice nucleation will be treated as water saturated when the deposition rates are calculated.

Both orders have physical interpretations. In the first scenario, ice nucleation produces a spatially inhomogeneous distribution of ice within a grid box by adding a small amount of ice to the previously liquid-only part of the grid box. Most of the ice resides in the ice-only region and any preexisting mixed-phase region. The fate of this ice is then dominated by the deposition rate outside of the freshly nucleated mixed-phase region.

In the second scenario, ice nucleation acts as a "flag," or indicator, identifying grid boxes where all the liquid cloud should be mixed phase. This corresponds to assuming that ice is uniformly distributed throughout the subgrid ice cloud volume. Because a larger fraction of ice will experience water-saturated conditions, when the nucleation-temperature threshold is crossed, the subsequent increase in ice mass could be very rapid.

5. Results of sensitivity tests

a. Sensitivity to riming, depositional growth, and turbulent mixing

1) Comparison to Moderate Resolution Imaging Spectroradiometer

In this section, the cloud-top heights simulated by the model sensitivity tests are compared to the estimated cloud-top height retrieved by the Moderate Resolution Imaging Spectroradiometer (MODIS). Figure 2 shows the effects of each of the process-rate parameterization changes on the model cloud-top height.[1] Only the region

[1] For each column, we define the model cloud-top height to be the greatest height at which the total condensed water content falls below $10^{-6}\,\mathrm{kg\,kg^{-1}}$. This value was chosen because it corresponds to the practical limit of in situ observations Cotton et al. (2012) and gives a reasonable level of condensate from which to estimate cloud top height for this case.

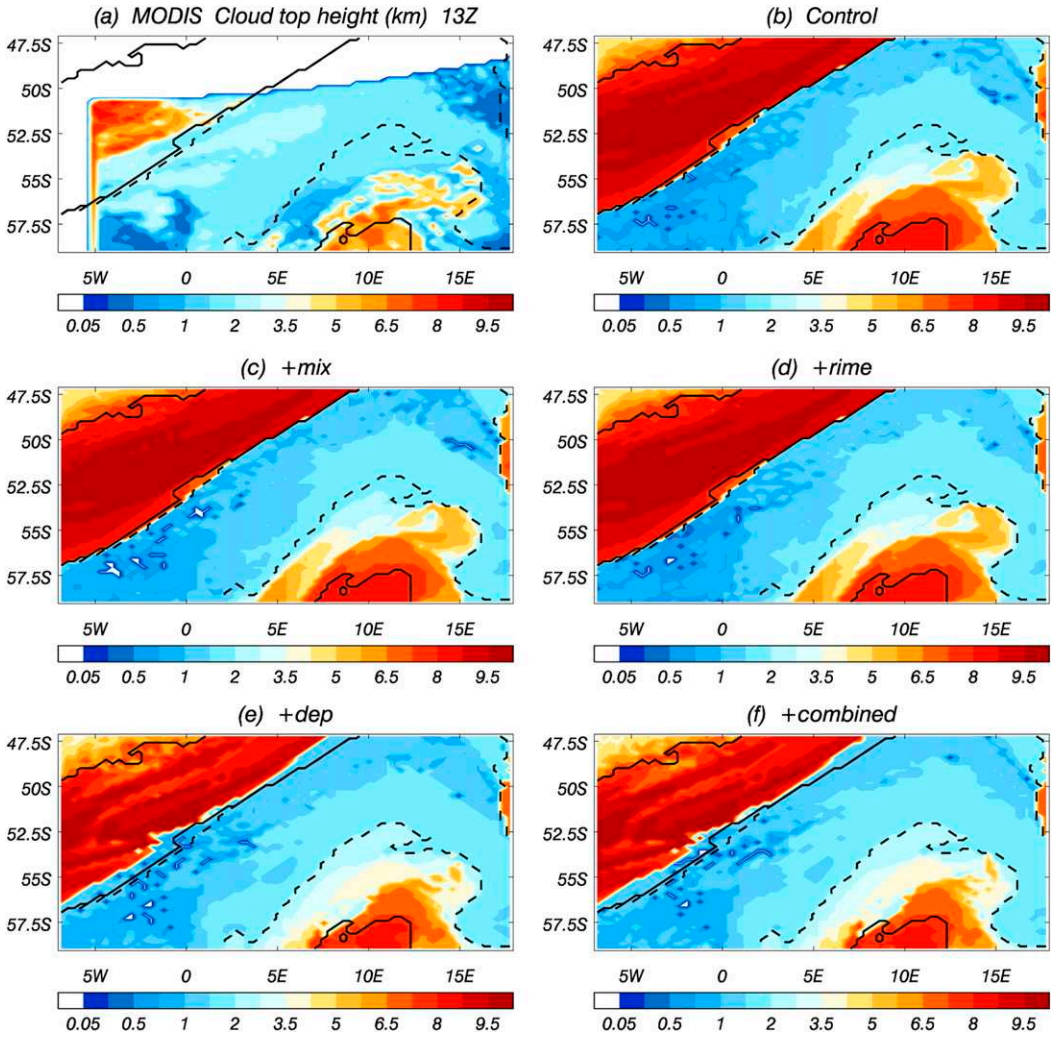

FIG. 2. Cloud-top height for (a) the MODIS retrieval, (b) the control model, and the experiment configurations with (c) no turbulent mixing of ice, (d) the modified riming-rate parameterization, (e) the modified deposition-rate parameterization, and (f) the combined set of parameterization changes. Only the region around the stratiform cloud layer is shown. The black cloud-top height contours show where all the models have cloud tops below 2 km (dashed line) and below 8 km (solid line). The color scale uses a level spacing of 250 m up to 1.25 km and 750 m above that. Any values below 50 m (i.e., small areas with no cloud) are shown in white.

immediately surrounding the stratiform cloud layer is shown. For reference, two cloud-top height contours are also shown: the solid line bounds the region where all the simulations have cloud-top heights $Z_h < 8$ km; the dashed line shows where all models have $Z_h < 2$ km.

Figure 2a shows the MODIS cloud-top height product. (The data were obtained from https://ladsweb.nascom.nasa.gov for an overpass time of 1325 UTC. The Collection 6 data from the *Aqua* orbital platform are used; Platnick et al. 2015.) Note that the data only partly covers the subdomain, but it includes the majority of the cold-air region. An artifact occurs on the western edge of the domain due to interpolation onto the latitude–longitude grid of the model.

Compared to MODIS, the control model (Fig. 2b) shows a combination of biases. Although, in this respect, it must be noted that uncertainties are known to exist in the observations: for example, Holz et al. (2008) showed that the MODIS retrieval tends to overestimate cloud-top height for low clouds, compared to the Cloud–Aerosol Lidar with Orthogonal Polarization (CALIOP) retrieval, and underestimate for optically thin high clouds. There is a large region of boundary layer cloud, with observed cloud tops between 1 and 2 km, for which the model clouds are too low. In the southeast quadrant of the domain, the observations show the stratus becoming punctuated by scattered, higher cloud tops. The control model produces midlevel convection in this

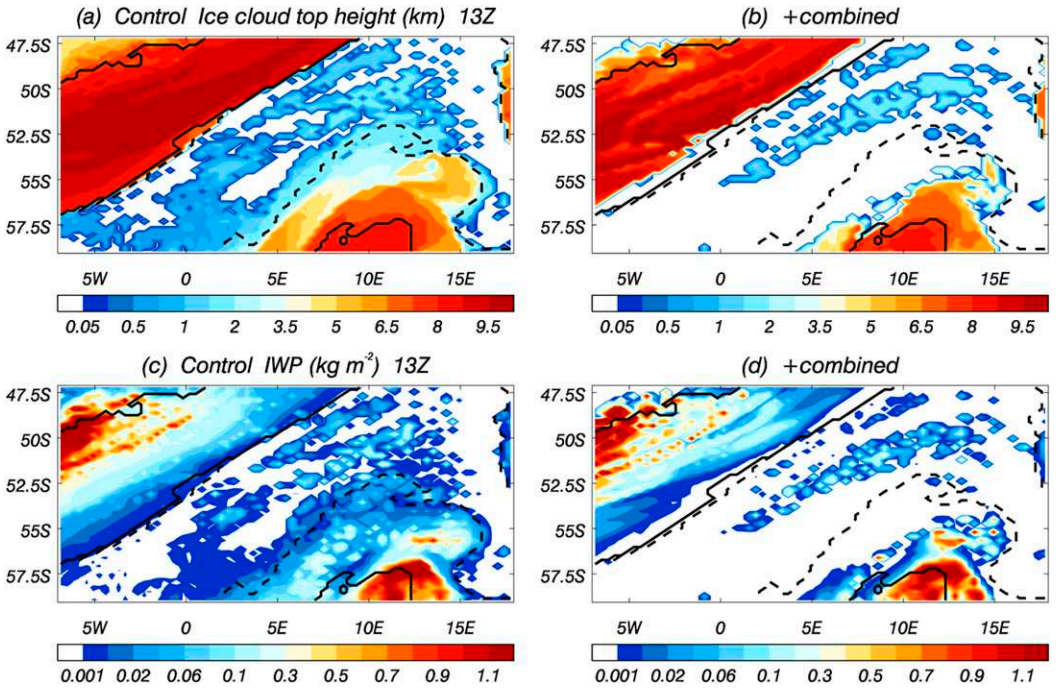

FIG. 3. (top) Ice cloud-top height and (bottom) ice water path for (a),(c) the control model and (b),(d) the experiment with the combined set of changes. The cloud-top-height color scale is as in Fig. 2. For IWP the level spacing is 0.01 kg m^{-2} up to 0.02 kg m^{-2} and then 0.02 kg m^{-2} up to 0.1 kg m^{-2}, above which it is 0.1 kg m^{-2}. Any values of LWP below 0.001 kg m^{-2} appear white.

region, with cloud tops frequently reaching above 5 km. These higher cloud tops cover a larger area than in the satellite retrievals. Around 10°E, on the southern edge of the domain, the encroaching warm front can be seen in both the observations and the model. Finally, in the northwest of the domain, the second warm front is either misplaced relative to its observed position or has too much high cloud associated with it.

The effects of the parameterization changes on model cloud-top height are shown in Figs. 2c–f. Removing the turbulent mixing of ice (Fig. 2c) and changing the riming parameterization (Fig. 2d) have very little effect on cloud-top height. The deposition-rate experiment (Fig. 2e) slightly increases the cloud-top heights in the stratus region and reduces the amount of midlevel cloud in the southeast quadrant. Figure 2f shows that effect of the combined changes. Overall, it is the deposition-rate change which dominates in terms of the effect on cloud-top height.

The changes in cloud-top height are related to changes in the amount of ice cloud. To investigate these effects we can define an ice cloud–top height, analogous to the total cloud-top height, as the maximum height at which the mass of ice falls below 10^{-6} kg kg^{-1}. Figures 3a and 3b show the effect on ice cloud-top height of the combined changes (changes to mixing, riming, and ice deposition). The area covered by ice cloud has been reduced. This is consistent with the deposition-rate change enhancing sublimation of ice and removing some ice cloud from the system.

As well as altering the vertical extent of ice in the simulations, the parameterization changes also affect the ice water path (IWP). Figures 3c and 3d show the changes in ice water path that accompany the changes in cloud-top height. The effect of the combined set of changes is mainly to remove low IWCs (IWPs less than 0.02 kg m^{-2}), with relatively low ice cloud tops, from the system. These clouds may be physically unrealistic features of the control model, but in situ ice measurements would be required to draw that conclusion.

The effects of the changes on cloud-top properties can be evaluated further by considering cloud-top temperature and phase. Figure 4 compares the histograms of cloud-top temperature for the control model and the combined experiment to the MODIS retrieval. The combined experiment (blue line) shows an increase in the fraction of colder cloud tops and a corresponding decrease in cloud tops warmer than −10°C. Overall, this gives a distribution of cloud-top temperatures that is closer to the MODIS retrievals than the control model (solid black line).

Figure 5 compares model-derived cloud-top phase (defined according to whether the calculated cloud top for ice is above, below, or in the same model vertical grid box

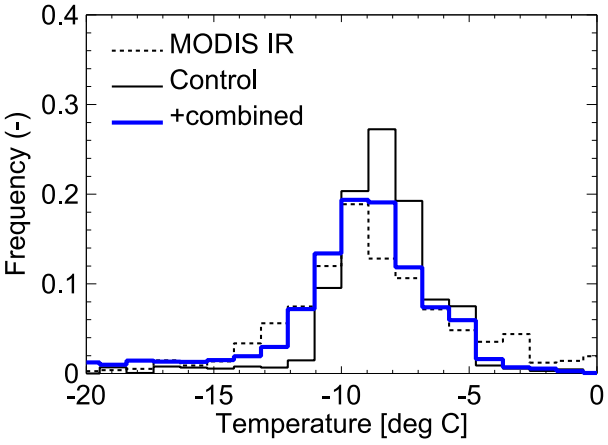

FIG. 4. Cloud-top-temperature histograms from the MODIS retrieval (dashed line), the control model (solid black line), and the experiment with the combined microphysics changes (solid blue line).

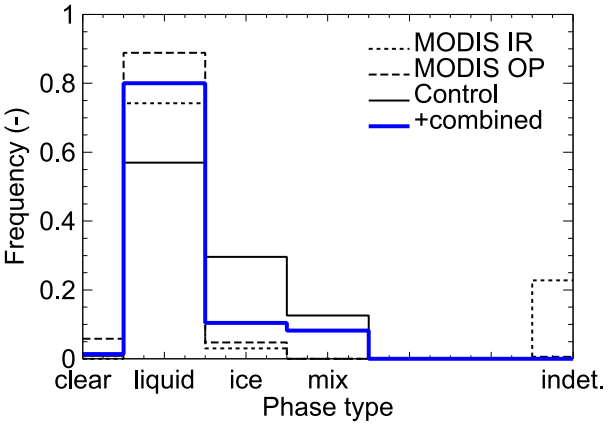

FIG. 5. Cloud-top-phase histograms from the MODIS retrieval (dashed line), the control model (solid black line), and the experiment with the combined microphysics changes (solid blue line).

as the liquid cloud top) to the MODIS retrievals. The "phase types" (clear sky, liquid, ice, mixed phase, and undetermined), on the horizontal axis, correspond to the definitions used in the two MODIS cloud-top phase products: Cloud-Top Phase Infrared (MODIS IR), short-dashed line; Cloud-Top Phase Optical Properties (MODIS OP), long-dashed line. Of the two products, the optical-properties-based estimate has less "uncertain" pixels and makes more frequent diagnosis of liquid-only cloud tops. Taken together, the products provide a pair of estimated bounds against which to compare the simulations. However, the prevalence of undetermined pixels in MODIS IR makes it difficult to draw definitive conclusions and there are known to be large uncertainties in the retrieval of cloud-top phase from satellite measurements (Huang et al. 2012, 2015a; Bodas-Salcedo et al. 2016). For example, Bodas-Salcedo et al. (2016) compared different methods for identifying cloud-top phase and found that a climatology based solely on MODIS underestimated the frequency of occurrence of liquid cloud tops by up to 30%, for cloud-top temperatures between −20° and 0°C, compared to methods which combined MODIS with information from *CloudSat–CALIPSO* (Kato et al. 2011). These differences are likely regime dependent, being due to either low-water-content clouds or thin cirrus overlying low-level liquid cloud. Huang et al. (2012, 2015a) also reported large uncertainties in cloud-top phase from different satellite-derived products.

From Fig. 5, it is clear that the combined changes increase the frequency of liquid cloud tops relative to the control model. At the same time, the changes reduce the prevalence of mixed-phase and ice cloud tops, which (subject to the caveat that the undetermined pixels could be mixed phase or ice) gives a better representation of the MODIS histogram.

To investigate the vertical distribution of cloud, Fig. 6 shows profiles of the area-weighted averages of the diagnostic subgrid cloud fraction from each of the models. The area-averaged value for each model is less than one because of fractional subgrid cloudiness and is, therefore, smaller than the area covered by grid boxes that contain some cloud. Two regions are selected: Fig. 6a shows the region of low-level, boundary layer clouds, where all the models have cloud-top heights, $Z_h < 2$ km, and Fig. 6b shows the region of midlevel convection, where $2 \le Z_h < 8$ km for all the models.

In the low clouds, the liquid cloud fractions (solid lines) are increased by the riming (red) and deposition-rate (green) changes. Turning off the turbulent mixing (not shown) has a much smaller effect. The changes in ice cloud fraction (dashed lines) are smaller: the riming change reduces the ice cloud fraction throughout the boundary layer; the deposition-rate change mainly affects the ice cloud where the liquid cloud fraction is low since, otherwise, the deposition rate is dominated by the mixed-phase regions.

By contrast, Fig. 6b shows that the ice cloud fractions are considerably reduced if midlevel convective clouds are present. The reduction is due to the deposition-rate change, which has evaporated low-IWC, midlevel ice clouds. Because of seeding from above by ice, reducing the amount of midlevel ice cloud also alters the amount of ice lower down in the atmosphere. In terms of the changes to the liquid cloud fraction in the $2 \le Z_h < 8$ region, riming dominates at heights below 2 km (where the LWCs are relatively high). Above 2 km, where there is less liquid cloud, riming is correspondingly less influential and the deposition-rate change dominates because the ice-only cloud fraction increases.

2) COMPARISON TO AMSR2

Model biases in the amount of liquid water in the simulations can be assessed against microwave-frequency

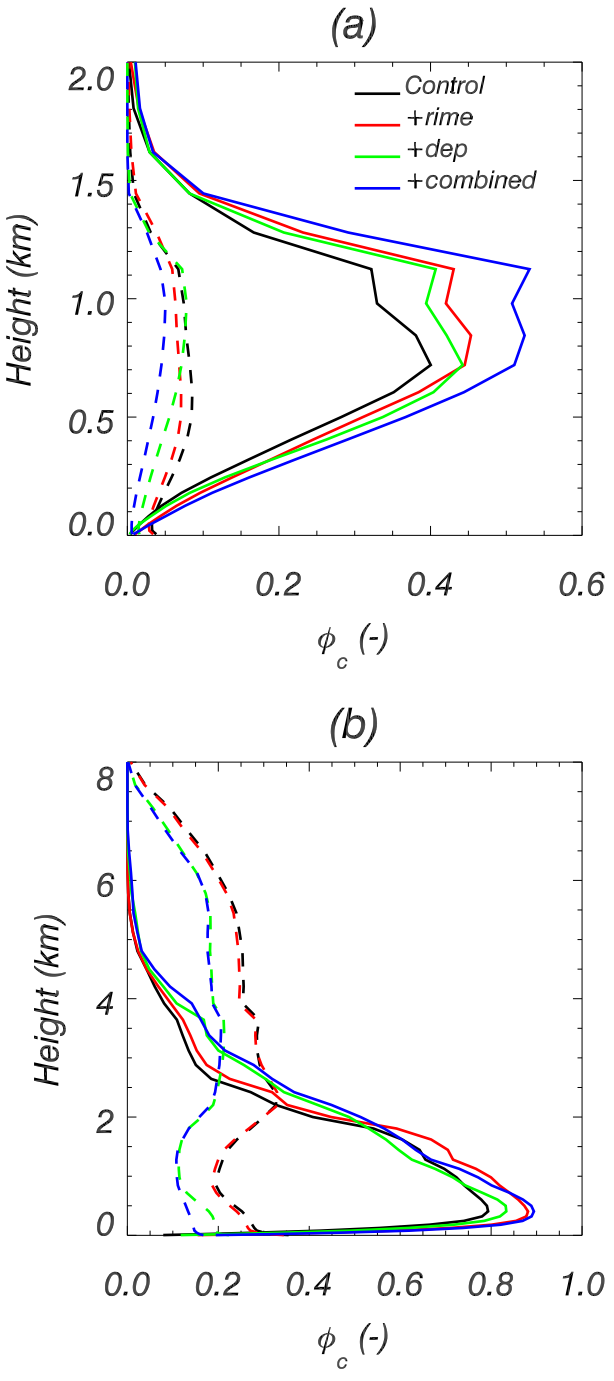

FIG. 6. Vertical profiles of area-averaged cloud fraction for the models. The averaging regions are where all the models have cloud-top heights (a) below 2 km and (b) between 2 and 8 km. The solid lines show liquid cloud fraction and the dashed lines show ice cloud fraction.

satellite retrievals. Figure 7 shows the effects on model liquid water path (LWP), compared to the AMSR2 observations (Fig. 7a). As in Fig. 2, the contour lines show where, for all the models, $Z_h < 8$ km (solid line) and $Z_h < 2$ km (dashed line). The control model (Fig. 7b) has too little liquid water in the region where stratiform cloud was observed. Where the model cloud tops are between 2 and 8 km, the model LWPs are too high. This is consistent with the excess of midlevel cloud in this region, compared to the MODIS retrieval. Note that the estimated error in the AMSR2 retrieval is reported to be 2–3 g m^{-2} (Lebsock and Su 2014), although the partitioning of liquid into cloud and rain is a potential source of uncertainty for heavily precipitating systems.

Figures 7c–f show the effects of the parameterization changes. Preventing boundary layer mixing of ice (Fig. 7c) has very little effect on the cloud LWP. Modifying the riming rates (Fig. 7d) makes liquid water more prevalent throughout the domain. An additional sensitivity test, which is not included here, demonstrates that this change is mainly a result of the reduced ice particle riming area and that the value of the threshold liquid water content for the onset of riming is less important. The effect of the deposition-rate change (Fig. 7e) is smaller and preferentially affects the $2 \leq Z_h < 8$ km region, where ice has been removed by the enhanced sublimation rates. Figure 7f shows that the combination of all three changes resembles the sum of the riming- and deposition-rate changes.

To investigate the vertical distribution of the changes in cloud liquid water content, Fig. 8 shows the vertical profiles of condensed water content for each of the experiments. In the low cloud (Fig. 8a), the liquid water contents (solid lines) are increased by the riming and deposition-rate changes. The same trends can be seen in below 2 km in the midlevel convective region (Fig. 8b). In comparison, the IWCs (dashed lines) are less sensitive—a feature that we will return to in the discussion.

3) COMPARISON TO CLOUDS AND THE EARTH'S RADIANT ENERGY SYSTEM

The increased LWCs of the clouds will affect the solar radiation reflected back to space. Estimates of the outgoing, top-of-atmosphere (TOA) shortwave (SW) and longwave (LW) fluxes can be obtain from the Clouds and the Earth's Radiant Energy System (CERES) Fast Longwave and Shortwave Radiative Flux (FLASHFlux) level 2, version B, data product, described by Kratz et al. (2014) (data obtained from https://eosweb.larc.nasa.gov). Typical uncertainties for these measurements are 5 W m^{-2} for the SW flux and 3 W m^{-2} for the LW flux (Loeb et al. 2007).

Figure 9 shows the impact of the combined set of changes on the outgoing radiative fluxes, compared to CERES (Figs. 9a,b). To emphasize the changes to the boundary layer clouds, a mask is applied so that the fluxes are only shown where $Z_h < 8$ km for all the models. The

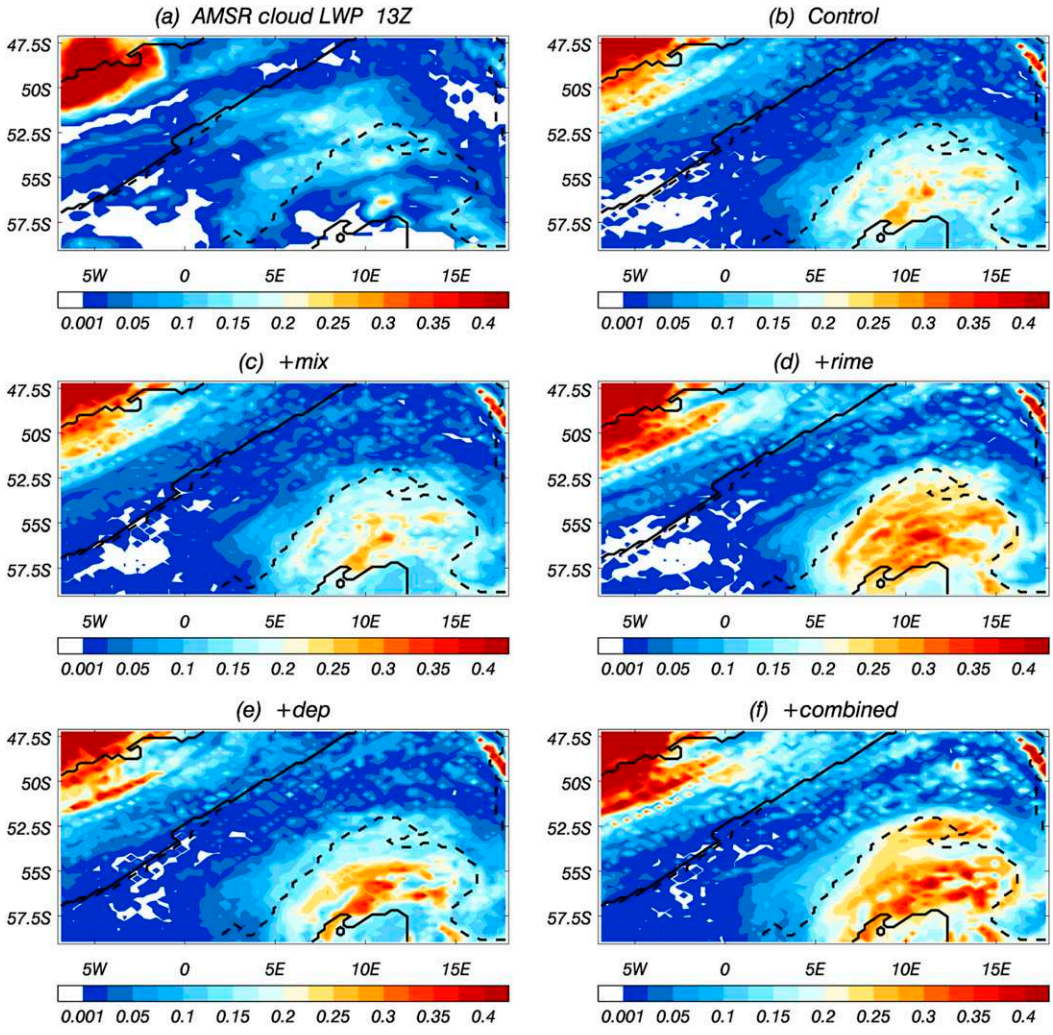

FIG. 7. Liquid water paths ($kg\,m^{-2}$) for (a) AMSR2, (b) the control model, and (c)–(f) the four experiment configurations. The black cloud-top-height contours show where all the models have cloud tops below 2 km (dashed line) and below 8 km (solid line). The color scale uses a constant level spacing of $0.025\,kg\,m^{-2}$. Any values below $0.001\,kg\,m^{-2}$ are shown in white.

higher LWPs in the experimental configuration lead to increased outgoing SW fluxes and corresponding reductions in outgoing LW flux. In both models, the clouds are too bright in the region of midlevel convection, which is consistent with the LWPs in this region being too large.

More details can be obtained by comparing the frequency distributions of the outgoing fluxes, shown in Fig. 10. To remove the influence of frontal clouds, the distributions are constructed using only grid boxes within the data mask shown in Fig. 9. The frequency distributions show that the model radiative biases have two causes. First, there are too many high-LWP clouds, leading to an excess of reflected SW fluxes above $600\,W\,m^{-2}$. Second, not enough of the ''dark'' sea surface is obscured by stratiform cloud, so too little SW is reflected between 200 and $600\,W\,m^{-2}$ and too much between 0 and $200\,W\,m^{-2}$ (this also accounts for the positive bias in the LW frequency distribution).

Figure 10b shows that the parameterizations changes improve the low-irradiance part of the SW histograms by covering more of the sea surface with cloud. The SW histogram is also improved between 500 and $600\,W\,m^{-2}$ because of the increase in the brightness of stratiform clouds seen in Fig. 9. However, the LWCs of the brightest clouds have increased further, which makes the bias in SW above $600\,W\,m^{-2}$ worse. Figure 10a shows a corresponding shift in the LW distribution toward lower irradiances.

b. Sensitivity to ice-nucleation temperature

In section 4d we described a set of sensitivity experiments for the parameterization of ice nucleation. These tests involve changes to ice-nucleation temperature in

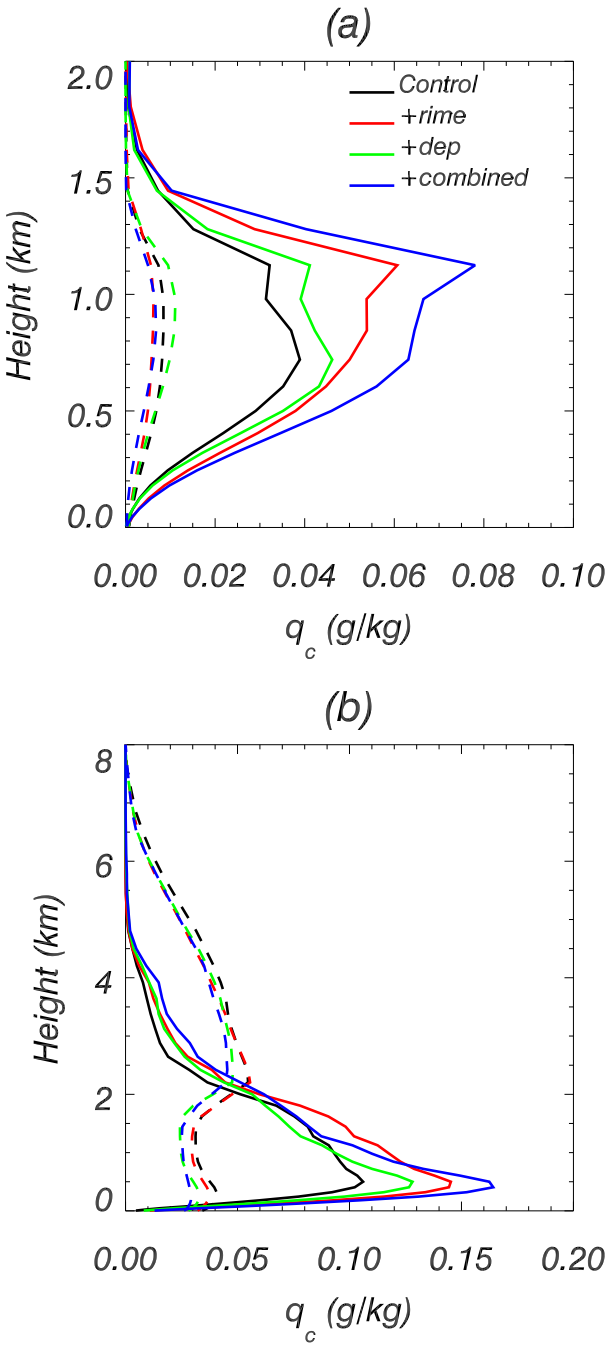

FIG. 8. Vertical profiles of area-averaged condensed water content for the models. The averaging regions are as in Fig. 6. The solid lines show liquid water content and the dashed lines show ice water content.

combination with changes to the ordering of the microphysical processes. We first assess the sensitivity of the control configuration to varying ice-nucleation temperature. Figure 11 shows frequency distributions of outgoing SW and LW flux for the control ($T_n = -10$°C) and several experiments. The red lines shows the histograms for $T_n = 0$°C with the default ice-nucleation parameterization (see section 4d). There is very little difference between the $T_n = 0$°C and the control distributions. This is surprising, given that $T_n = 0$°C is warm enough for ice formation throughout the boundary layer. The outgoing LW fluxes are similarly insensitive to ice-nucleation temperature, when the default ice-nucleation assumptions are used. We also note that another experiment with $T_n = -40$°C produced TOA flux histograms that are very similar to those shown for $T_n = -10$°C. Taken together with the cloud-top temperature histograms shown in Fig. 4 (which show that $T_n = -10$°C is a typical cloud-top temperature), this suggests that, even for $T_n = -10$°C, ice nucleation has relatively little effect on the amount of ice and liquid in the model clouds in this case.

The green lines in Fig. 11 show the frequency distributions for $T_n = 0$°C when the modified ice-nucleation assumptions (i.e., the different process order) are used. In this model, the subgrid humidity partition is recalculated after ice nucleation occurs. With the modified assumptions, the $T_n = 0$°C experiment shows a decrease in the outgoing SW flux. Most of the grid boxes that have high irradiances in the control model have been redistributed into intermediate-irradiance parts of the SW frequency distribution.

The redistributed grid boxes correspond to regions where the LWPs were too high in the control model. This can be seen in Fig. 12, which compares ice cloud–top height (top row), LWP (middle row), and IWP (bottom row) in the three experiments with $T_n = 0$°C. Comparing Figs. 12a, 12d, and 12g to the corresponding figures for the control configuration (Figs. 3a,c, and 7b) shows how little the simulated clouds have been affected by increasing T_n from −10° to 0°C, if the default ice-nucleation assumptions are used. By contrast, Figs. 12b, 12e, and 12h show that, if the modified ice-nucleation assumptions are used, then the LWC decreases and the amount of ice cloud increases if $T_n = 0$°C.

With the default nucleation assumptions, any mixed-phase cloud created on a given time step is assumed to have a very low IWC and hence is negligible in terms of its effect on depositional growth. The only effect of ice nucleation is to increment IWC by a small amount. This method could deplete liquid water gradually, over several time steps, but it appears to be ineffective at doing so.

The changes in cloud are more pronounced with the modified assumptions because, on a subgrid scale, the ice mass is uniformly distributed throughout the ice cloud, whenever $T_n \leq 0$°C. This implies that a greater fraction of the ice mass in a grid box is growing in water-saturated conditions, compared to a simulation with the

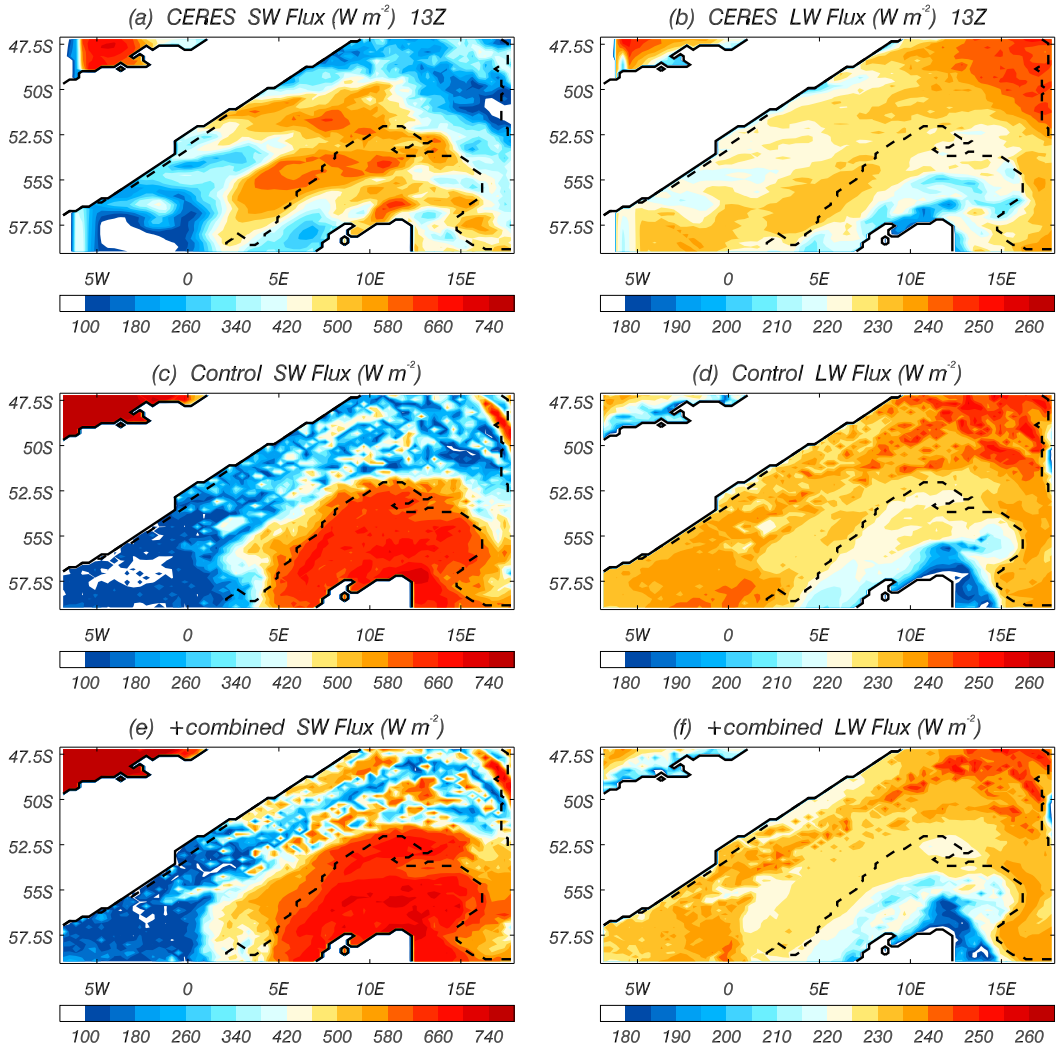

FIG. 9. Outgoing TOA (left) SW flux and (right) LW flux for (a),(b) CERES FLASHFlux, (c),(d) the control model, and (e),(f) the experiment with the combined set of changes.

default assumptions. The deposition process is therefore more rapid and, because deposition is a sink of ''total water'' (liquid and vapor combined), this reduces the amount of liquid condensation that is diagnosed by the cloud scheme.

As a final experiment, to examine the interaction of ice-nucleation temperature and process-rate changes, Figs. 12c, 12f, and 12i show the effect of combining T_n = 0°C, with the modified assumptions, and the combined physics changes from section 5a. The effect of these changes is similar to that obtained when they are applied to the control model: increased LWP and a decrease in ice cloud cover. The blue histograms in Fig. 11 show that the effect of these changes on the TOA radiative fluxes is to reduce the frequency of intermediate-brightness grid boxes by redistributing them back into the high-irradiance part of the histogram.

6. Applications to global models

In this section we assess the applicability of the convective-scale modeling results to the development of global models. In particular, it is interesting to consider whether the parameterization changes tested can reduce large-scale model biases in the Southern Ocean region. More generally, it is useful to understand the extent to which the high- and low-resolution simulations show similar biases.

We will consider only the change to the riming rate because this change has the firmest basis in observations and is also the change most likely to be applicable to models other than the Unified Model. It is also the change that is the most targeted toward affecting only supercooled stratus clouds. For example, the deposition-rate change can be shown to also affect ice growth in

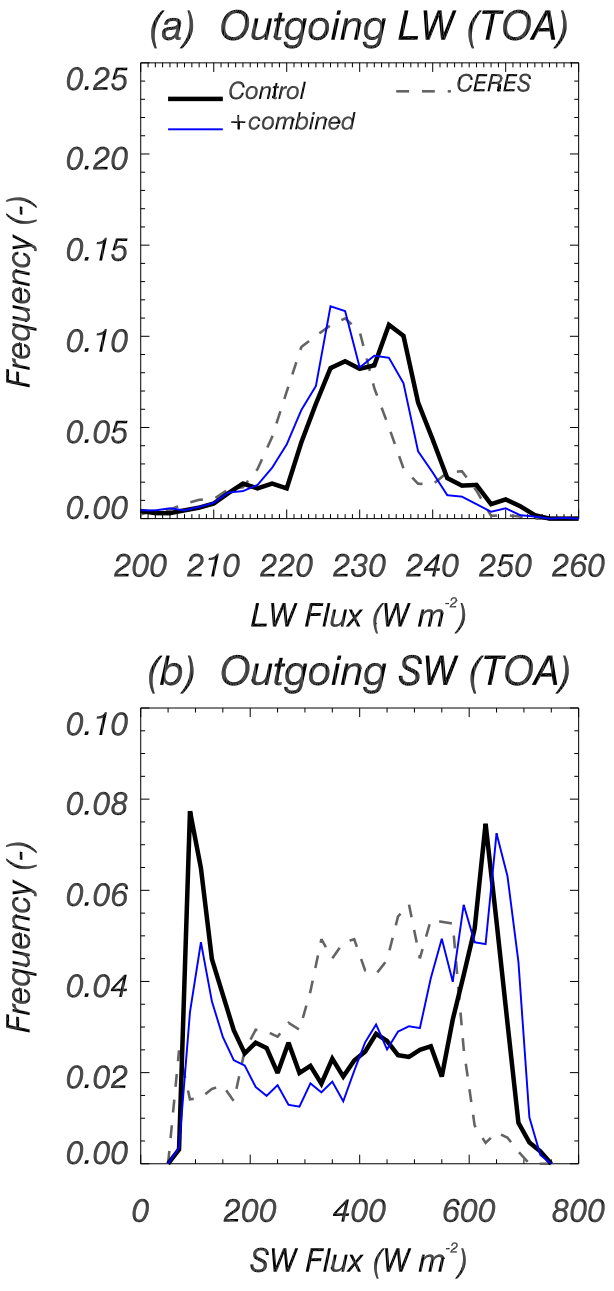

FIG. 10. Histograms of (a) outgoing TOA LW flux and (b) outgoing TOA SW flux for the control model, combined experiment, and the CERES observations. The histograms are constructed for the region where all the models have cloud tops below 8 km.

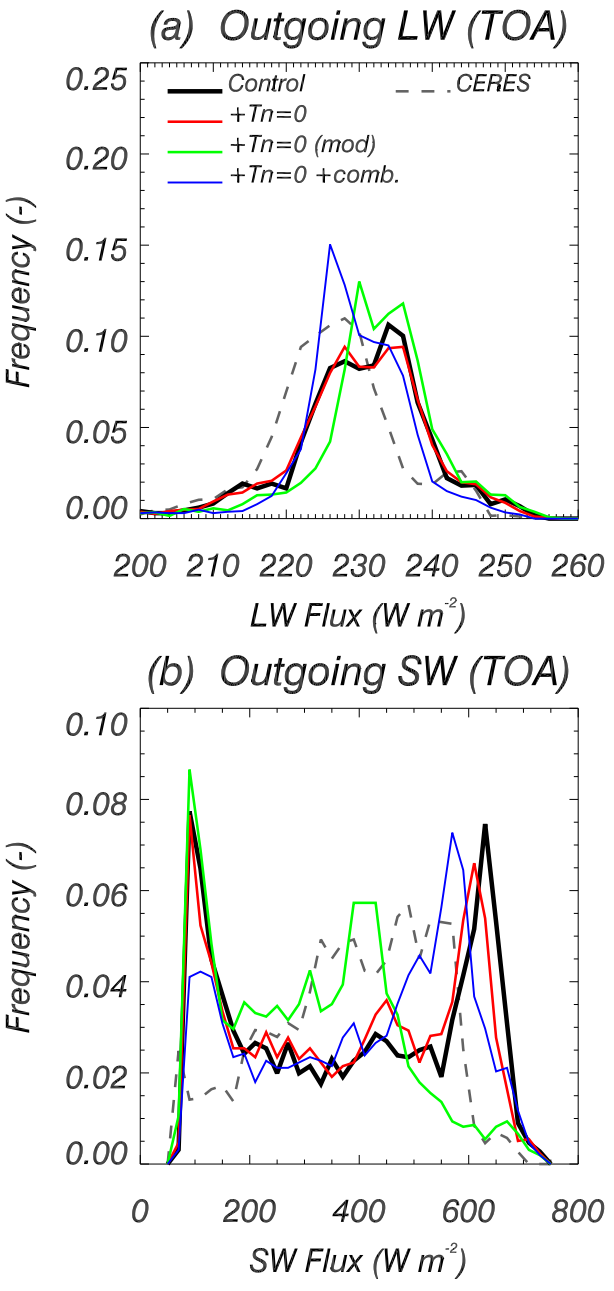

FIG. 11. Histograms of (a) outgoing TOA LW flux and (b) outgoing TOA SW flux, for the control model, ice-nucleation-temperature experiments, and the CERES observations. The histograms are constructed for the region where all the models have cloud tops below 8 km.

cirrus clouds, which makes the effects on climate simulations difficult to analyze. The effects of the ice-nucleation sensitivities on global models will also be omitted because in global models, ice nucleation in the microphysics scheme needs to be considered together with ice nucleation in parameterized convective clouds and in the model's prognostic cloud-fraction scheme.

The riming-rate change was tested in two low-resolution model simulations: a 22-km-resolution LAM, with the same domain and boundary conditions as the high-resolution simulations, and a 20-yr climate integration. Moreover, to assess the robustness of the results, the low-resolution LAM and climate model have different model physics, although the ice-microphysical

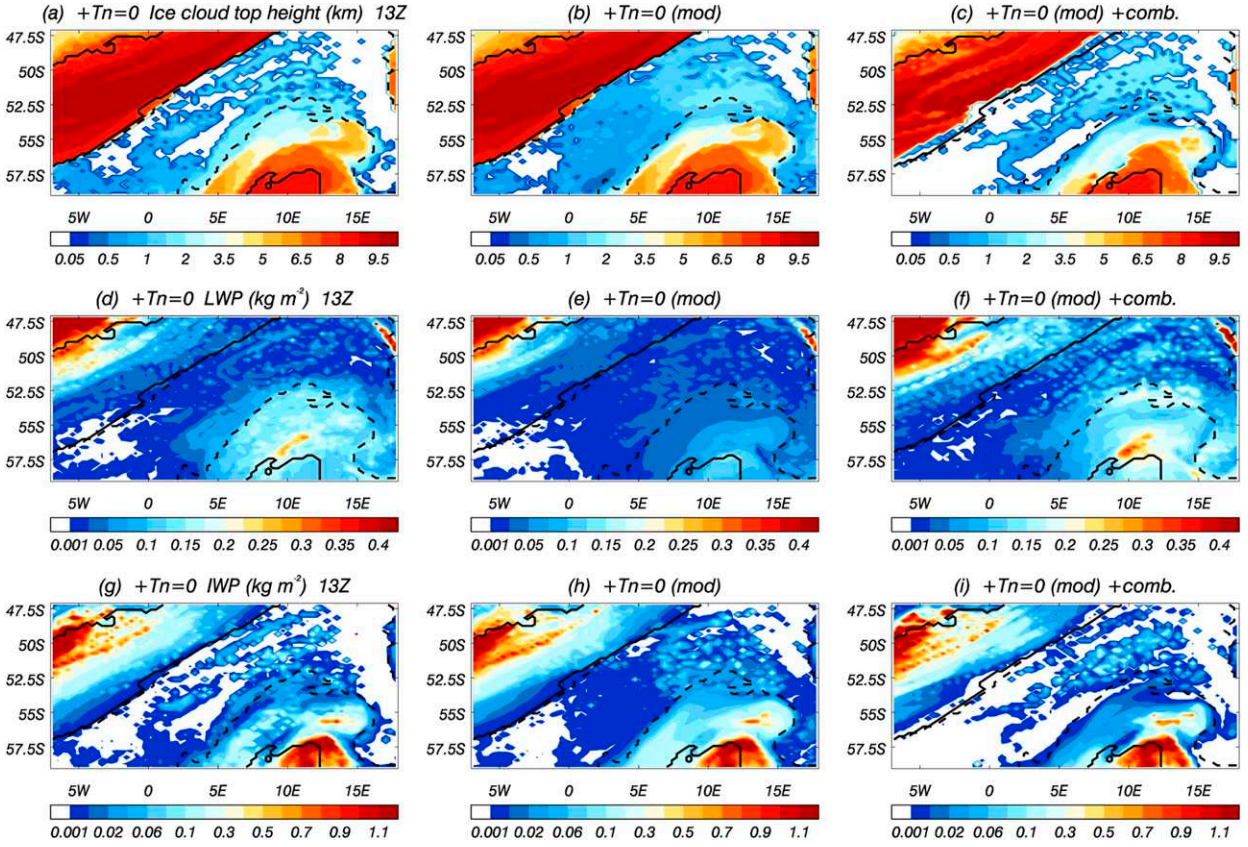

FIG. 12. (a)–(c) Ice cloud–top height, (d)–(f) liquid water path, and (g)–(i) ice water path for (a),(d),(g) $T_n = 0$°C; (b),(e),(h) $T_n = 0$°C with the modified ice-nucleation assumptions; and (c),(f),(i) $T_n = 0$°C with the modified ice nucleation and combined parameterization changes. The color scales used are as in Figs. 2, 3, and 7.

processes and properties are parameterized identically in the two configurations. The LAM is based on GA6.1, but with the ice microphysics changed to be the same as the high-resolution simulations (this also means that the LAM has the same model physics as the global NWP simulation, which was used to drive the high-resolution runs, and the climate model). In particular, the parameterizations of riming, ice nucleation, and ice depositional growth are the same in the low- and high-resolutions LAMs. The ice-microphysical properties (mass, fall speed, and size distribution) are also identical in the two resolutions. Because the low-resolution LAM has the same microphysics configuration as the high-resolution model, the resolution dependence of the sensitivity experiments can be investigated. Here we interpret ''resolution dependence'' in a broad sense that includes effects arising from interactions with other model components that are present in the low-resolution configuration but are absent in the high-resolution model—for example, the convection parameterization. The climate simulation was performed with the Met Office Global Atmosphere 7 (GA7) configuration with a resolution of N96. This model also has the same microphysics configuration as the two LAMs.

Figure 13 shows the histograms of outgoing LW and SW flux for the low-resolution LAM with the control configuration and an experiment including the change to the riming rate. As was done in Figs. 10 and 11, the histograms are constructed for the region where both the models have cloud tops below 8 km. We note that this masked region differs slightly from the masked region for the high-resolution models in Figs. 10 and 11 because the cloud-top heights differ between the simulations. This accounts for differences in the difference seen in the histogram of the observations between Figs. 10 and 13.

Comparison with Fig. 10 reveals obvious differences in the nature of the cloud biases between the low- and high-resolution configurations. This is to be expected, given significant differences in model setup: not only is convection parameterized at 22-km grid spacing, but the low-resolution model uses a prognostic cloud scheme (Wilson et al. 2008), whereas the high-resolution model uses an empirical relationship to diagnose liquid cloud

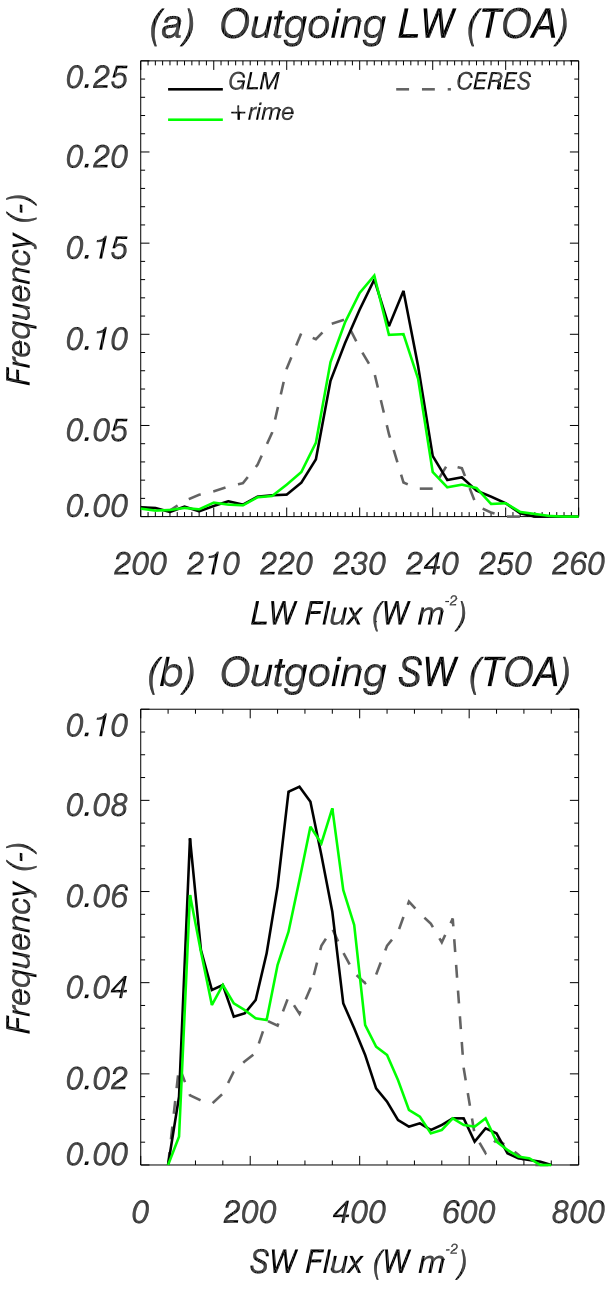

FIG. 13. Histograms of (a) outgoing TOA LW flux and (b) outgoing TOA SW flux, for the control model and riming-rate experiment for the 22-km-resolution LAM. The histograms are constructed for the region where both the models have cloud tops below 8 km.

fraction and condensate. An obvious difference in bias is that the low-resolution model does not have a peak in reflected SW between 600 and 800 W m^{-2} and instead peaks around 300 W m^{-2} (where the convection-permitting model has relatively few grid boxes). The "bright peak" in the high-resolution model at 600–800 W m^{-2} is due to the midlevel convective clouds generated by that model, which are not present to the same extent in the satellite observations or the low-resolution model. Because the low-resolution model does not produce as much of this cloud type, it represents the high-irradiance part of the observed histograms relatively well.

However, there are also similarities between the model histograms. For example, the LW histograms are biased in the same way because of the lack of stratiform liquid cloud in both sets of models. This lack of liquid water is also evident in the SW histograms between 400 and 600 W m^{-2}, where both resolutions of model contribute too few grid boxes. In the low-resolution model, these grid boxes instead contribute to the histograms around 300 W m^{-2}, indicating that the stratiform clouds that exist in the model are not reflective enough.

At both resolutions, the models respond to the change in riming rate in the same manner. The liquid water contents of the clouds increase, so there is a shift in the SW histogram toward higher values of irradiance and a corresponding opposite shift in the LW histogram.

Figure 14 puts these changes into a regional-climate context. It shows the effect of the riming-rate change on the 20-yr mean state for high latitudes in the Southern Hemisphere in December–February. Figure 14a shows the bias in outgoing SW flux in the experiment configuration relative to CERES Energy Balanced and Filled (CERES-EBAF). The bias has a meridional gradient that appears to be due to the poleward traversal of the Southern Hemisphere storm track. At lower latitudes the negative bias gives way to a (smaller) positive bias. In the experiment, the negative bias in the polar region is reduced by up to 6 W m^{-2}, compared to the bias in the control model (Fig. 14b). However, equatorward of Drake Passage, the existing positive SW flux bias is made worse by the changes. Figure 14c shows the change in outgoing SW between the experiment and control. The changes correlate well with the increased LWPs shown in Fig. 14d. A global analysis of the changes (not shown) shows that the Northern Hemisphere is similarly affected, particularly in the midlatitude storm tracks and Arctic. Given the absence of significant negative SW biases at northern high latitudes, the changes are not beneficial to those regions. The reasons for the strong meridional gradient in the bias remain obscure at this stage, but it can be speculated that, over time, the GCM has been developed to have microphysics that is "tuned" toward producing relatively darker Northern Hemisphere clouds, which have a greater prevalence of ice clouds and less to supercooled liquid (Bodas-Salcedo et al. 2016). This may have been done, for example, by raising the ice-nucleation temperature (to represent relatively ice-nuclei-rich environments) and using ice

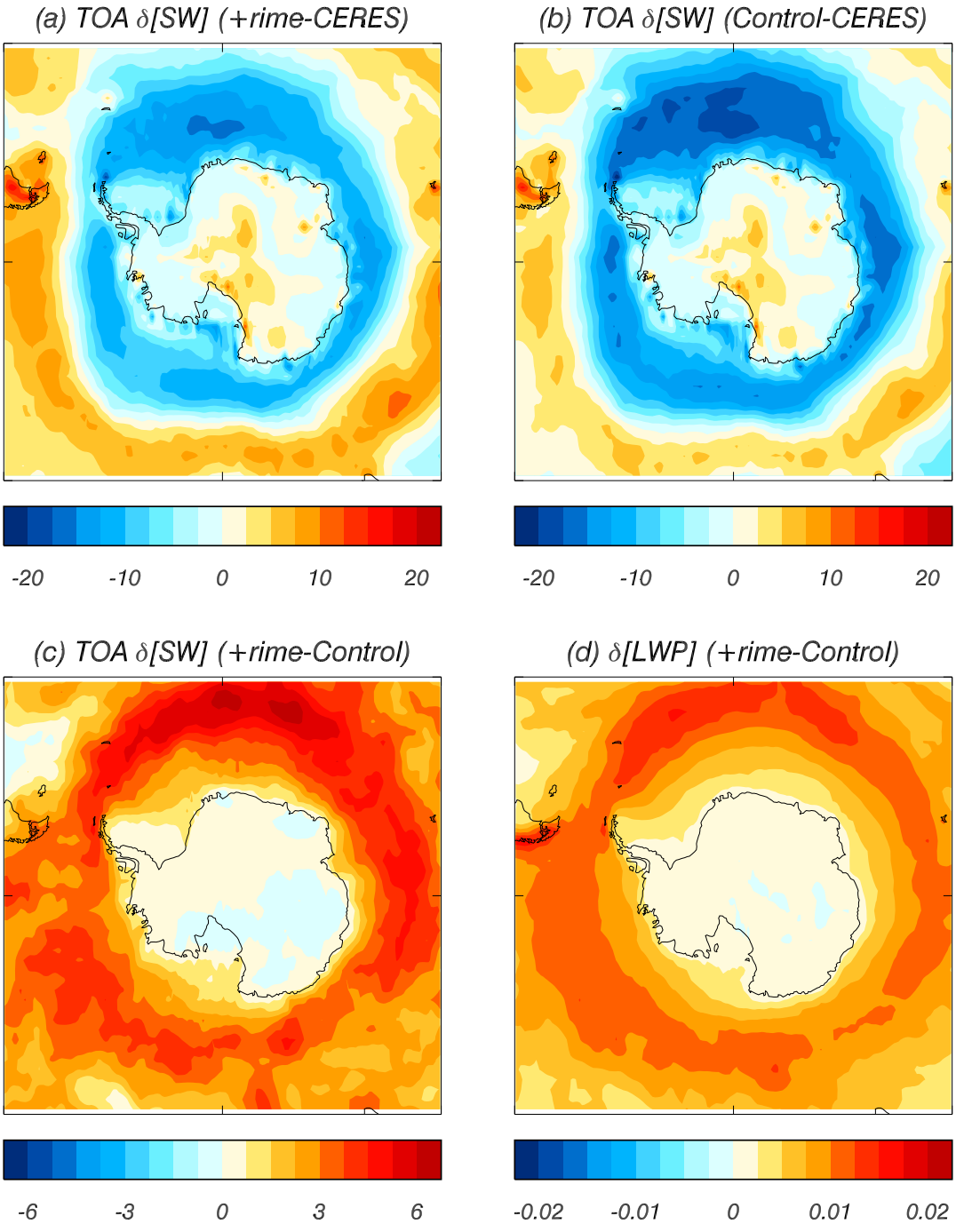

FIG. 14. The effect of the riming-rate change on the 20-yr-mean climate at high latitudes in the Southern Hemisphere: (a) outgoing SW flux bias for the riming-rate experiment, compared to CERES-EBAF, (b) the control model bias, (c) SW flux differences between the experiment and control, and (d) the associated changes in LWP.

microphysical properties (e.g., area–diameter relations) and subgrid-scale assumptions (e.g., subgrid humidity distributions), which have the effect of enhancing the production of ice (by riming and deposition) and reducing liquid water content. This would have the unwanted side effect of misrepresenting clouds in more pristine environments, such as over the Southern Ocean. Conversely, changes that increase the liquid water contents are likely to adversely affect the brightness of simulated Northern Hemisphere and low-latitude clouds.

7. Discussion

In this section we will summarize the effects of the parameterization changes on the average properties of the simulations. We show that small changes in IWP can induce large changes in LWP and discuss how this is related to the sensitivity of precipitation rate to IWC (Senior and Mitchell 1993; Ceppi et al. 2016). Figures 15a and 15b compare the condensed water paths and TOA radiative fluxes, for all the experiments, averaged over the region where all the models have cloud tops below 8 km. The AMSR2 and CERES observations are shown by the black triangle on Fig. 15a and the horizontal black line on Fig. 15b. The different sensitivities give a range of LWPs, and this is accompanied by changes in the outgoing SW and LW fluxes, with higher LWPs corresponding to brighter clouds that are less transmissive of upwelling LW radiation. It is interesting to note that the sensitivity experiments produce a range to results that span the observations, suggesting that in order to minimize the biases a balance needs to be found between process-rate changes and ice-nucleation temperature.

The square symbols in Fig. 15 show the LWPs and SW fluxes for the 22-km-resolution, local-area model with the GA6-based model configuration (black square) and riming experiment (red square). This is consistent with the findings of previous studies that global models underpredict the observed liquid water and SW flux (Bodas-Salcedo et al. 2012; Williams et al. 2013; Bodas-Salcedo et al. 2014). This is in contrast to the majority of the high-resolution experiments where liquid water content is, on average, overpredicted because of the high LWPs of midlevel convective clouds. The direction of the response in LWP is the same as for the corresponding high-resolution experiment, but the amount of extra liquid water produced is much less. The differences in the magnitude of the response may be due to difference in cloud types or differences in other parameterizations between the resolutions. It may also be due to the interaction of ice microphysics with resolved circulations in the 2.2-km model, which are subgrid scale in the low-resolution LAM. We also note that the smaller LWP response of the 22-km model is consistent with that model having the lowest ice water content: there is less ice in the simulations to be affected by the riming-rate change. Figure 15b suggests that models with the highest IWPs also have the largest LWP response to changes that reduce the production of ice.

It is interesting to note that the range of IWPs produced by the models is smaller than the range of LWPs. Although increases in liquid are accompanied by decreases in the amount of ice, the magnitude of the changes in IWP are considerably smaller. Other studies have also reported that IWC is less sensitive than LWC to changes in mixed-phase clouds. For example, Klein et al. (2009) compared a number of different large-eddy and single-column models for a case study of Arctic

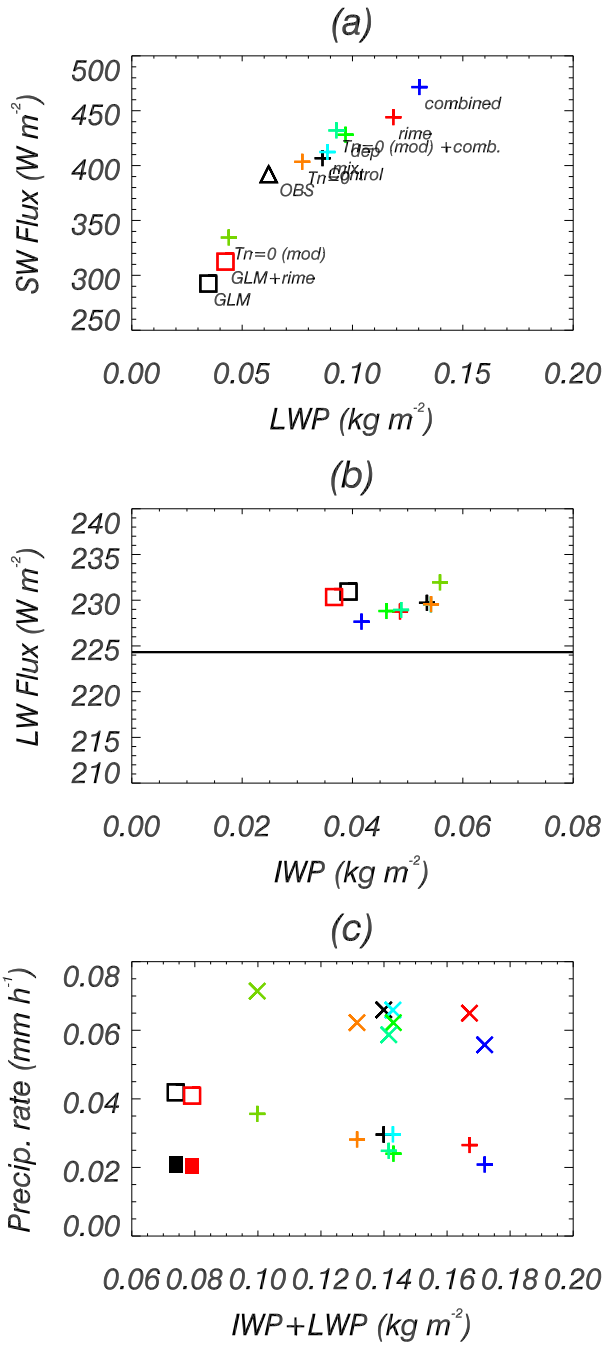

FIG. 15. Comparisons of simulated quantities, area averaged over the region where, for all models, the cloud-top height is below 8 km. (a) LWP and outgoing SW flux at TOA. (b) IWP and outgoing LW flux. (c) Condensed water path, surface total precipitation rate (crosses and squares), and surface snowfall rate (plus signs and filled boxes). The square symbols show the variables for the 22-km-resolution LAMs.

stratus and found that the range of IWCs sampled was smaller than the range of LWCs. Ceppi et al. (2016) considered the global changes in condensed water content in general circulation models (GCMs) due to climate change. They found LWP to be approximately 3 times more sensitive than IWP, at 60°S, to temperature changes (see their Fig. 1). A similar response was reported in the earlier studies by Choi et al. (2014) and Tsushima et al. (2006). Ceppi et al. (2016) also noted that the absence of a compensating decrease in IWP, to counteract the increased LWP in warmer climates, drives an overall increase in total cloud water at middle to high latitudes. The same behavior can be seen in Fig. 15 for the high-resolution simulations studied here.

Ceppi et al. (2016) attribute the smaller climate sensitivity of ice, compared to liquid water, to the argument articulated by Senior and Mitchell (1993) that precipitation is more efficient when it forms via mixed-phase processes (because ice particles exposed to water saturation will grow rapidly compared to liquid droplets). In this picture, a parameterization change that increases IWP at the expense of LWP should also increase the precipitation rate. Moreover, because increased precipitation will be accompanied by a decrease in condensed water (liquid plus ice), the change must affect IWC and LWC in an asymmetric fashion (Ceppi et al. 2016).

A detailed analysis of the hydrology of the model is complicated because the simulations are not in steady states. However, Fig. 15c shows that our results are at least consistent with the above interpretation: for the most part, models with higher condensed water paths also exhibit smaller surface snowfall rates (shown by the plus signs) and total surface precipitation rates (crosses). This is consistent with parameterization changes that inhibit the growth of ice leading to lower precipitation rates that, in turn, lead to higher liquid water contents.

8. Conclusions

We have investigated the sensitivity of mixed-phase clouds, in the cold-air outflow from a simulated Southern Ocean cyclone, to the parameterization of ice microphysics and boundary layer mixing.

A riming parameterization that includes the effects of nonspherical ice particles was shown to increase the liquid water contents of mixed-phase boundary layer clouds. A change to the deposition-rate parameterization, based on simplifying the assumptions for the subgrid-scale correlations between ice and water vapor, also increases the amount of liquid water cloud. The mixing of ice by the model boundary layer scheme was found to have little effect on the simulations. The changes made are physically based and may therefore be useful for global-model development and bias reduction in climate simulations. We also identified a novel lack of sensitivity to ice-nucleation temperature, which can be traced to physical (but implicit) assumptions about subgrid heterogeneity.

We evaluated the model sensitivity tests against remotely sensed measurements of LWP (from AMSR2); cloud-top height, phase, and temperature (from MODIS); and top-of-atmosphere radiative fluxes from CERES. The comparisons revealed significant model biases, in terms of the prevalence of different cloud types (stratiform cloud and convective cloud), the liquid water contents of these clouds, and their overall radiative impact in the simulations. The statistical distribution of cloud-top properties and the LWPs in the model stratiform clouds were found to be improved by those sensitivities that enhanced LWC. Although significant biases remain, it is encouraging that the range of sensitivities spanned across the observations for the case, suggesting that further tuning of the model could bring significant improvements.

When the nature of the biases in the high-resolution simulations was compared to those in low-resolution (convective parameterized) runs, both similarities and differences were revealed. For example, because of an excess of midlevel convection at high resolution, the convection-permitting simulations typically overestimated LWC while the low-resolution models underestimated. However, both resolutions of the model showed the same deficit of liquid water content in stratiform cloud and the direction (but not the magnitude) of the model response to the riming-parameterization change was independent of resolution.

From the parameterization changes developed, the change to the riming rate was selected for testing in an AMIP simulation, where it was shown to increase the liquid water paths over the Southern Ocean and, consequently, increase the shortwave radiation reflected to space by up to 6 $\mathrm{W\,m^{-2}}$ in the annual mean. A significant further reduction in the bias can be obtained by modifying the parameterization of the large-scale condensation of liquid water in mixed-phase clouds, as addressed by Furtado et al. (2016), following the ideas of Field et al. (2014b). The remaining bias may be due to further microphysical effects (of the kinds considered here), aerosol-direct effects, aerosol–cloud interactions, and other factors, such as errors in near-surface winds.

The sensitivity of the simulations to ice-nucleation temperature was found to be surprisingly subtle and related to the ordering of microphysical processes within a model time step. The default ordering of processes was found to give very little sensitivity to T_n, over a wide range,

because the deposition rates were not able to respond easily to increases in mixed-phase volume due to ice nucleation. A different process order was shown to give a much higher sensitivity to the value of T_n. The importance of process order was interpreted in terms of subgrid assumptions about the spatial distribution of ice inside each grid box. We have not investigated the effect on ice nucleation of the initial mass of ice seeded by ice-nucleation parameterization. This could also affect the sensitivity of the model to T_n. However, it is interesting that, for a fixed value of the seed mass, the microphysical process order can determine the model response to T_n changes. The physical interpretation given for the process order could be applicable to other atmospheric models and might be important when comparing the ice-nucleating characteristics of different microphysics schemes.

Although ice water path varied with the changes made, it was found to be less sensitive than LWP: a finding that is consistent with other studies. The relative lack of sensitivity of the ice may arise because precipitation rates respond readily to changes in cloud ice, so small changes in IWC can induce large changes in the hydrology of the system.

Future work will focus on fully understanding the implications of the changes described here for global-model simulations. In particular, it will be interesting to perform a detailed analysis of the effects of riming, deposition, and ice nucleation on the global climate and their implications of climate projection.

Acknowledgments. The authors performed this work as part of their regular job duties as employees of the Met Office (GB). KF and PRF acknowledge the benefit to this work of helpful discussions with Patrick Hyder, Alejandro Bodas-Salcedo, Keith Williams, Dan Copsey, John Edwards, Adrian Lock, and the other members of the Met Office Southern Ocean Process Evaluation Group. AMSR data are produced by Remote Sensing Systems and were sponsored by the NASA AMSR-E Science Team and the NASA Earth Science Making Earth Science Data Records for Use in Research Environments (MEaSUREs) Program. Data are available online (at www.remss.com).

REFERENCES

Bodas-Salcedo, A., K. D. Williams, P. R. Field, and A. P. Lock, 2012: The surface downwelling solar radiation surplus over the Southern Ocean in the Met Office model: The role of midlatitude cyclone clouds. *J. Climate*, **25**, 7467–7486, doi:10.1175/JCLI-D-11-00702.1.

——, and Coauthors, 2014: Origins of the solar radiation biases over the Southern Ocean in CFMIP2 models. *J. Climate*, **27**, 41–56, doi:10.1175/JCLI-D-13-00169.1.

——, P. G. Hill, K. Furtado, K. D. Williams, P. R. Field, J. C. Manners, P. Hyder, and S. Kato, 2016: Large contribution of supercooled liquid clouds to the solar radiation budget of the Southern Ocean. *J. Climate*, **29**, 4213–4228, doi:10.1175/JCLI-D-15-0564.1.

Ceppi, P., D. L. Hartmann, and M. J. Webb, 2016: Mechanisms of the negative shortwave cloud feedback in middle to high latitudes. *J. Climate*, **29**, 139–157, doi:10.1175/JCLI-D-15-0327.1.

Choi, Y.-S., C.-H. Ho, C.-E. Park, T. Storelvmo, and I. Tan, 2014: Influence of cloud phase composition on climate feedbacks. *J. Geophys. Res. Atmos.*, **119**, 3687–3700, doi:10.1002/2013JD020582.

Cotton, R. J., and Coauthors, 2012: The effective density of small ice particles obtained from in situ aircraft observations of midlatitude cirrus. *Quart. J. Roy. Meteor. Soc.*, **139**, 1923–1934, doi:10.1002/qj.2058.

Field, P. R., A. J. Heymsfield, and A. Bansemer, 2007: Snow size distribution parameterization for midlatitude and tropical ice clouds. *J. Atmos. Sci.*, **64**, 4346–4365, doi:10.1175/2007JAS2344.1.

——, R. J. Cotton, K. McBeath, A. P. Lock, S. Webster, and R. P. Allan, 2014a: Improving a convection-permitting model simulation of a cold air outbreak. *Quart. J. Roy. Meteor. Soc.*, **140**, 124–138, doi:10.1002/qj.2116.

——, A. A. Hill, K. Furtado, and A. Korolev, 2014b: Mixed-phase clouds in a turbulent environment. Part 2: Analytic treatment. *Quart. J. Roy. Meteor. Soc.*, **140**, 870–880, doi:10.1002/qj.2175.

Fletcher, N. H., 1962: *The Physics of Rainclouds*. Cambridge University Press, 386 pp.

Furtado, K., P. R. Field, A. Baran, and R. Cotton, 2015: The sensitivity of simulated high clouds to ice crystal fall speed, shape and size distribution. *Quart. J. Roy. Meteor. Soc.*, **141**, 1546–1559, doi:10.1002/qj.2457.

——, ——, I. A. Boutle, C. R. Morcrette, and J. Wilkinson, 2016: A physically based subgrid parametrization for the production and maintenance of mixed-phase clouds in a general circulation model. *J. Atmos. Sci.*, **73**, 279–291, doi:10.1175/JAS-D-15-0021.1.

Harimaya, T., 1975: The riming properties of snow crystals. *J. Meteor. Soc. Japan*, **53**, 384–392.

He, J., and B. J. Soden, 2016: The impact of SST biases on projections of anthropogenic climate change: A greater role for atmosphere-only models? *Geophys. Res. Lett.*, **43**, 7745–7750, doi:10.1002/2016GL069803.

Heymsfield, A. J., and L. M. Miloshevich, 2003: Parameterizations for the cross-sectional area and extinction of cirrus and stratiform ice cloud particles. *J. Atmos. Sci.*, **60**, 936–956, doi:10.1175/1520-0469(2003)060<0936:PFTCSA>2.0.CO;2.

Holz, R. E., S. A. Ackerman, F. W. Nagle, R. Frey, S. Dutcher, R. E. Kuehn, M. A. Vaughan, and B. Baum, 2008: Global Moderate Resolution Imaging Spectroradiometer (MODIS) cloud detection and height evaluation using CALIOP. *J. Geophys. Res.*, **113**, D00A19, doi:10.1029/2008JD009837.

Huang, Y., S. T. Siems, M. J. Manton, A. Protat, and J. Delanoe, 2012: A study on the low-altitude clouds over the Southern Ocean using the DARDAR-MASK. *J. Geophys. Res.*, **117**, D18204, doi:10.1029/2012JB009424.

——, ——, ——, and G. Thompson, 2014: An evaluation of WRF simulations of clouds over the Southern Ocean with A-train observations. *Mon. Wea. Rev.*, **142**, 647–667, doi:10.1175/MWR-D-13-00128.1.

——, C. N. Franklin, S. T. Siems, M. J. Manton, T. Chubb, A. Lock, S. Alexander, and A. Klekociuk, 2015a: Evaluation of boundary-layer cloud forecasts over the Southern Ocean in a limited-area numerical weather prediction system using

in situ, space-borne and ground-based observations. *Quart. J. Roy. Meteor. Soc.*, **141**, 2259–2276, doi:10.1002/qj.2519.

——, A. Protat, S. T. Siems, and M. J. Manton, 2015b: A-Train observations of maritime midlatitude storm-track cloud systems: Comparing the Southern Ocean against the North Atlantic. *J. Climate*, **28**, 1920–1939, doi:10.1175/JCLI-D-14-00169.1.

Jones, J. M., and Coauthors, 2016: Assessing recent trends in high-latitude Southern Hemisphere surface climate. *Nat. Climate Change*, **6**, 917–926, doi:10.1038/nclimate3103.

Kato, S., and Coauthors, 2011: Improvements of top-of-atmosphere and surface irradiance computations with CALIPSO-, CloudSat-, and MODIS-derived cloud and aerosol properties. *J. Geophys. Res.*, **116**, D19209, doi:10.1029/2011JD016050.

Klein, S. A., and Coauthors, 2009: Intercomparison of model simulations of mixed-phase clouds observed during the ARM Mixed-Phase Arctic Cloud Experiment. I: Single-layer cloud. *Quart. J. Roy. Meteor. Soc.*, **135**, 979–1002, doi:10.1002/qj.416.

Korolev, A., and P. R. Field, 2008: The effect of dynamics on mixed-phase clouds: Theoretical considerations. *J. Atmos. Sci.*, **65**, 66–86, doi:10.1175/2007JAS2355.1.

——, G. A. Isaac, S. G. Cober, J. W. Strapp, and J. Hallett, 2003: Microphysical characterization of mixed-phase clouds. *Quart. J. Roy. Meteor. Soc.*, **129**, 39–65, doi:10.1256/qj.01.204.

Kratz, D. P., P. W. Stackhouse Jr., S. K. Gupta, A. C. Wilber, P. Sawaengphokhai, and G. R. McGarragh, 2014: The Fast Longwave and Shortwave Flux (FLASHFlux) data product: Single-scanner footprint fluxes. *J. Appl. Meteor. Climatol.*, **53**, 1059–1079, doi:10.1175/JAMC-D-13-061.1.

Lebsock, M., and H. Su, 2014: Application of active spaceborne remote sensing for understanding biases between passive cloud water path retrievals. *J. Geophys. Res. Atmos.*, **119**, 8962–8979, doi:10.1002/2014JD021568.

Lock, A. P., A. R. Brown, M. R. Bush, G. M. Martin, and R. N. B. Smith, 2000: A new boundary-layer mixing scheme. Part I: Scheme description and single-column model tests. *Mon. Wea. Rev.*, **128**, 3187–3199, doi:10.1175/1520-0493(2000)128<3187:ANBLMS>2.0.CO;2.

Loeb, N. G., S. Kato, K. Loukachine, N. Manalo-Smith, and D. R. Doelling, 2007: Angular distribution models for top-of-atmosphere radiative flux estimation from the Clouds and the Earth's Radiant Energy System instrument on the *Terra* satellite. Part II: Validation. *J. Atmos. Oceanic Technol.*, **24**, 564–584, doi:10.1175/JTECH1983.1.

McCoy, D. T., D. L. Hartmann, M. D. Zelinka, P. Ceppi, and D. P. Grosvenor, 2015: Mixed-phase cloud physics and Southern Ocean cloud feedback in climate models. *J. Geophys. Res. Atmos.*, **120**, 9539–9554, doi:10.1002/2015JD023603.

Morrison, H., G. de Boer, G. Feingold, J. Harrington, M. D. Shupe, and K. Sulia, 2012: Resilience of persistent Arctic mixed-phase clouds. *Nat. Geosci.*, **5**, 11–17, doi:10.1038/ngeo1332.

Platnick, S., S. A. Ackerman, M. D. King, K. Meyer, W. P. Menzel, R. E. Holz, B. A. Baum, and P. Yang, 2015: MODIS atmosphere L2 cloud product (06_L2). NASA MODIS Adaptive Processing System, Goddard Space Flight Center. [Available online at https://modaps.modaps.eosdis.nasa.gov/services/about/products/c6/MYD06_L2.html.]

Sallée, J.-B., E. Shuckburgh, N. Bruneau, A. J. S. Meijers, T. J. Bracegirdle, Z. Wang, and T. Roy, 2013: Assessment of Southern Ocean water mass circulation and characteristics in CMIP5 models: Historical bias and forcing response. *J. Geophys. Res. Oceans*, **118**, 1830–1844, doi:10.1002/jgrc.20135.

Senior, C. A., and J. F. B. Mitchell, 1993: Carbon dioxide and climate: The impact of cloud parameterization. *J. Climate*, **6**, 393–418, doi:10.1175/1520-0442(1993)006<0393:CDACTI>2.0.CO;2.

Tan, I., and T. Storelvmo, 2016: Sensitivity study on the influence of cloud microphysical parameters on mixed-phase cloud thermodynamic phase partitioning in CAM5. *J. Atmos. Sci.*, **73**, 709–728, doi:10.1175/JAS-D-15-0152.1.

Trenberth, K. E., and J. T. Fasullo, 2010: Simulation of present-day and twenty-first-century energy budgets of the southern oceans. *J. Climate*, **23**, 440–454, doi:10.1175/2009JCLI3152.1.

Tsushima, Y., and Coauthors, 2006: Importance of the mixed-phase cloud distribution in the control climate for assessing the response of clouds to carbon dioxide increase: A multi-model study. *Climate Dyn.*, **27**, 113–126, doi:10.1007/s00382-006-0127-7.

Turner, J., T. Bracegirdle, T. Phillips, G. Marshall, and J. Hosking, 2013: An initial assessment of Antarctic sea ice extent in the CMIP5 models. *J. Climate*, **26**, 1473–1484, doi:10.1175/JCLI-D-12-00068.1.

Wentz, F. J., T. Meissner, C. Gentemann, K. A. Hilburn, and J. Scott, 2014: Remote Sensing Systems GCOM-W1 AMSR2 Daily Environmental Suite on 0.25 deg grid, version 7.2. Remote Sensing Systems, accessed 2 February 2015. [Available online at http://data.remss.com/amsr2/bmaps_v07.2/y2014/m12/.]

Williams, K. D., and Coauthors, 2013: The Transpose-AMIP II experiment and its application to the understanding of Southern Ocean cloud biases in climate models. *J. Climate*, **26**, 3258–3274, doi:10.1175/JCLI-D-12-00429.1.

Wilson, D. R., and D. P. Ballard, 1999: A microphysically based precipitation scheme for the UK Meteorological Office Unified Model. *Quart. J. Roy. Meteor. Soc.*, **125**, 1607–1636, doi:10.1002/qj.49712555707.

——, A. C. Bushell, A. M. Kerr-Munslow, D. P. Jeremy, and C. J. Morcrette, 2008: PC2: A prognostic cloud fraction and condensation scheme. I: Scheme description. *Quart. J. Roy. Meteor. Soc.*, **134**, 2093–2107, doi:10.1002/qj.333.